

TITLE

by

Nikolaus Hartman

A dissertation submitted to The Johns Hopkins University in conformity with the
requirements for the degree of Doctor of Philosophy.

Baltimore, Maryland

Month, 2015

© Nikolaus Hartman 2015

All rights reserved

Abstract

I made like 2000 devices. This thesis probably is written about the 3 devices that worked in the summer of 2015.

Primary Reader: A Scientist

Secondary Reader: Another Scientist

Acknowledgments

Thanks! . . .

Dedication

This thesis is dedicated to ...

Contents

Abstract	ii
Acknowledgments	iii
List of Tables	ix
List of Figures	x
1 Introduction	1
1.1 Section	1
1.1.1 Subsection	1
1.2 Optional table of contents heading	2
1.2.1 Another subsection	2
1.2.1.1 Subsubsection	2
2 Electronic Properties of Carbon Nanotubes	3
2.1 Electronic Bandstructure of Graphene	3

CONTENTS

2.1.1	Graphene Lattice	4
2.1.2	Tight Binding Model	7
2.1.3	Low Energy Bandstructure of Graphene	12
2.2	Electronic Bandstructure of Carbon Nanotubes	14
2.2.1	Types of Carbon Nanotubes	18
2.2.2	Low Energy Bandstructure of Carbon Nanotubes	19
2.3	Carbon Nanotube Field Effect Transistors	21
2.4	Carbon Nanotube Quantum Dots	24
3	Carbon Nanotube Growth and Placement	31
3.1	Random Dispersion	31
3.1.1	Catalyst	32
3.1.2	Growth	32
3.1.3	Nanotube Placement	35
3.1.4	Conclusion	36
3.2	Catalyst Island Growth	37
3.2.1	Catalyst	38
3.2.2	Growth	40
3.2.3	Conclusion	42
3.3	Imaging Nanotubes	43
3.3.1	Atomic Force Microscopy	43
3.3.2	Electric Force Microscopy	45

CONTENTS

3.3.3	EFM Through PMMA	47
3.3.4	Scanning Electron Microscopy	48
3.4	Image Filtering	50
3.4.1	Histogram Equalization	50
3.4.2	Matched Filter Bank	53
3.4.2.1	Nanotube Profile Model	53
3.4.2.2	Filter Kernel	55
3.4.2.3	Filter Bank	57
4	Metallic Contacts to Carbon Nanotubes	62
5	Quantum Dots with Ferromagnetic Leads	63
6	Spin Transport in Tunable Ferromagnet/Superconductor Junction	64
A	Fabrication Details	65
A.1	Wafer Preparation	66
A.1.1	Selection and Cleaning	66
A.1.2	Optical Lithography	67
A.1.2.1	Projection Lithography	68
A.1.2.2	Mask Aligner	69
A.2	Device Design	71
A.3	Electron Beam Lithography	72

CONTENTS

A.3.1 Standard Recipe	73
A.3.2 Cold Development	74
A.4 Thin Film Deposition	75
A.4.1 Thermal Evaporation	75
A.4.2 Electron Beam Evaporation	76
A.4.3 Sputtering	77
A.4.4 Atomic Layer Deposition	78
A.4.5 Liftoff	80
A.5 Room Temperature Testing	81
A.5.1 Probe Station	81
A.5.2 Wire Bonding	82
B Measurement Details	85
Bibliography	86
Vita	92

List of Tables

3.1	Powder Catalyst	32
3.2	Patterned Catalysts	39
3.3	Matched Filter Bank Parameters	60
A.1	Standard PMMA/MIBK recipe	73
A.2	Cold developer recipe	74
A.3	Thermal evaporation materials	76

List of Figures

2.1	The real-space structure of the graphene lattice. Vectors \vec{a}_1 and \vec{a}_2 define the unit cell, which contains two atoms, highlighted in red and blue.	5
2.2	The reciprocal lattice of graphene. Vectors \vec{b}_1 and \vec{b}_2 define the Brillouin zone. The high symmetry points Γ , K , K' , and M are labeled..	6
2.3	(a) The π -bands of graphene calculated using a nearest neighbor tight binding model. (b) A contour plot of the upper band with the first Brillouin zone drawn. The bands meet at the three K and three K' points at the vertices of the Brillouin zone.	12
2.4	The real-space structure of a carbon nanotube. The nanotube unit cell is defined by the vectors \vec{C}_h and \vec{T}	15
2.5	The reciprocal lattice of a carbon nanotube, defined by the vectors K_1 and K_2	17
2.6	Two types of carbon nanotube bandstructure. The left plot shows a metallic (5,5) armchair nanotube. The right plot shows a semiconducting (4,2) chiral nanotube.	19
2.7	Schematic of a carbon nanotube field effect transistor.	21
2.8	Current versus gate voltage characteristics for three typs of CNTFET.	22
2.9	IV characteristics of a typical small band gap semiconducting CNT-FET. The current saturates at higher bias voltage, but is not typically measured due to avalanche breakdown of the devices. Inset: Current versus gate at a fixed bias for the same device.	23
2.10	R-T curve of a CNTFET cooled to 4 K	24
2.11	Quantum dot energy diagram.	25
2.12	Left: A quantum dot level resonant with the source/drain chemical potential. Right: The same device in the blockaded region.	27
2.13	Conductance as a function of applied gate voltage in a cobalt contacted nanotube quantum dot.	28
2.14	Left: A quantum dot level resonant with the drain chemical potential. Right: The same device in the blockaded region.	29

LIST OF FIGURES

2.15 Left: An IV curve at fixed gate voltage Right: Differential conductance measured at fixed gate voltage.	29
2.16 Conductance of a cobalt contacted nanotube quantum dot at 4K as a function of bias and gate voltages.	30
3.1 The tube furnace fitted with a 1" diameter quartz tube. The tube is sealed at both ends using 1" rubber tubing, cable clamps, and KF25 fittings. Gas flows from left to right in the picture. The gas flows out of the furnace into a mineral oil bubbler to keep hot hydrogen from reaching the air in the room. Gas then flows from the bubbler into the building exhaust.	33
3.2 The gas handling panel for our Lindberg tube furnace. Gas flow is from left to right.	34
3.3 A Si/SiO ₂ substrate with 1 μm Au markers. Left scale bar: 100 μm. Right scale bar: 20 μm	37
3.4 A Si/SiO ₂ substrate with 3 μm catalyst islands and Mo leads. Left scale bar: 100 μm. Right scale bar: 20 μm	38
3.5 A composite image made from several AFM height measurements of a sample with nanotubes dispersed over a substrate with 1.5 μm gold markers. The scale bar is 10 μm.	44
3.6 An EFM image of nanotubes dispersed over a substrate with 1.5 μm gold markers. The markers have been automatically located using the height data and highlighted in blue on the EFM image. The scale bar is 10 μm.	46
3.7 (a) Frequency data collected from an EFM scan of a catalyst island sample after nanotube growth. (b) Frequency data collected from an EFM scan of a similar sample. Prior to the scan this sample was coated with a 250 nm PMMA layer. Both scale bars are 10 μm.	48
3.8 A scanning electron micrograph of a catalyst island sample after nanotube growth. The scale bar is 10 μm.	49
3.9 An illustration of the histogram equalization process.	51
3.10 Top image is the original SEM image after a plane fit. Middle image shows the SEM image after histogram equalization. Bottom image shows the final result after gaussian smoothing. Plots on the right show the histogram of brightness values and cumulative distribution function at each step.	52
3.11 a) The original data set of SEM nanotube images used to create and optimize the matched filter bank. b) The same data set rotated and overlaid with extracted nanotube profiles.	54
3.12 a) Extracted nanotube profiles with linear background removed (blue). Fits to 3.1 (red). b) Distribution of k values extracted from profile fits. c) Distribution of straight nanotube section lengths.	56

LIST OF FIGURES

3.13 a) Original image. b) Final filtered image, which is the sum of the binary images in (d). c) The rotated kernels that form the full matched filter bank. d) Each rotated kernel applied to an image in (a).	58
3.14 Optimization of the matched filter bank threshold value.	59
3.15 Optimization of the matched filter bank threshold value.	61
A.1 Custom projection lithography setup in the JHU physics department cleanroom. (a) The arrows from left to right show the UV lamp, sliding UV filter, and mask holder. (b) A projection lithography mask and holder. The arrow shows the mask itself.	68
A.2 OAI mask aligner in the JHU physics department cleanroom. (a) The mask aligner. (b) A typical 3" chromium on glass mask.	70
A.3 Adobe Illustrator designs used for optical and electron beam lithography masks. (a) The pink outlines show the large molybdenum leads patterned with the mask aligner. Inside that pattern are the four $3\text{ }\mu\text{m}$ catalyst islands patterned with electron beam lithography. (b) An SEM micrograph of a sample after CVD growth fitted into the pattern. (c) A complete circuit design. In this case, the layers are normal metal (green), ferromagnet (purple), and superconductor (blue).	71
A.4 Zeiss EVO50 SEM with Raith control computer and external beam blanker.	72
A.5 The Markovic lab ALD reactor. Gas flow is from right to left.	78
A.6 (a) A substrate with catalyst islands and a few long nanotubes before patterning. (b) The same substrate after patterning and liftoff. Comparing the two images, it is clear that the use of sonication during liftoff has broken many of the nanotubes.	81
A.7 The Markovic lab probe station. Four sharp probes are located under an optical microscope. Each can be connected to external sources and measurements using BNC connectors.	82
A.8 (a) Kulicke and Soffa wire bonder. (b) An optical image of a completed device mounted in a chip carrier. (c) An SEM image detailing aluminum wires bonded to large gold leads.	83

Chapter 1

Introduction

Introduction to nanotubes, transport spectroscopy, and some stuff to tie together the various measurements made for this thesis.

Currently, this chapter contains a bunch of L^AT_EXreference material.

1.1 Section

This is a section. Here's a reference to a different section: 1.1.1.

1.1.1 Subsection

This is a subsection.

CHAPTER 1. OPTIONAL RUNNING CHAPTER HEADING

1.2 Section with

linebreaks in

the name

This is another section.

1.2.1 Another subsection

1.2.1.1 Subsubsection

1.2.1.1.1 HEADING LEVEL BELOW SUBSUBSECTION

And I quote:

La la la.

No indent after end of quote.

Another paragraph with a list:

- Item 1
- Item 2

Again, we don't indent here.

Chapter 2

Electronic Properties of Carbon

Nanotubes

Carbon nanotubes exhibit a variety of interesting material and electrical properties. Nanotubes can be used as mechanical oscillators, one dimensional conductors, and quantum dots, among many other applications. The work in this thesis takes advantage of the unique electronic and spin transport properties of carbon nanotubes. By starting with the graphene lattice, these properties are easily derived.

2.1 Electronic Bandstructure of Graphene

The electronic bandstructure of graphene was first calculated in 1947 by P.R. Wallace (CITE). This was done as part of an effort to understand the electronic structure

CHAPTER 2. PROPERTIES OF CNTS

of bulk graphite. In this paper, there is mention of the two lowest energy bands and the half filling of a single layer of carbon atoms. It was not until 1984 that Semenoff discussed the existence of a linear dispersion relation for low energy electronic excitations in single layers of carbon atoms (CITE). This was done by looking at a generic honeycomb lattice as an analoge of 2+1 dimensional electrodynamics. Semenoff found the low energy electronic band structure of the monoatomic honeycomb lattice matched that of Dirac fermions.

Graphene was first isolated on silicon wafers through mechanical exfoliation in 2004. The semimetallic characteristics were confirmed through measuring transistor curves and the charge carrier sign change through the Hall effect (CITE). Shortly after, the same research group confirmed the existance of low energy Dirac fermions in graphene (CITE).

Beginning with the structure of the monoatomic honeycomb lattice, and following the original work of Wallace, the electronic band structure of graphene will be derived below.

2.1.1 Graphene Lattice

As mentioned above, single layers of carbon atoms, graphene, form a honeycomb lattice. This lattice can be seen in Figure 2.1.

In Figure 2.1 the unit cell is defined by the two lattice vectors \vec{a}_1 and \vec{a}_2 . Each unit cell is comprised of two atoms. The honeycomb lattice can be thought of as to

CHAPTER 2. PROPERTIES OF CNTS

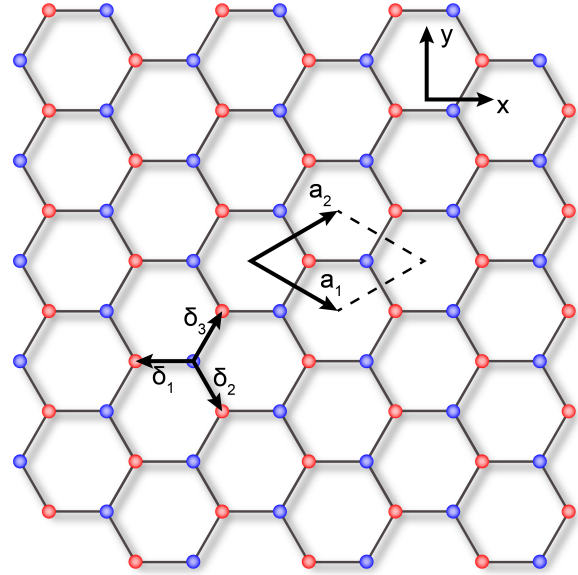


Figure 2.1: The real-space structure of the graphene lattice. Vectors \vec{a}_1 and \vec{a}_2 define the unit cell, which contains two atoms, highlighted in red and blue.

interpenetrating triangular sublattices. With that picture, the honeycomb unit cell contains one atom from each of the two sublattices, highlighted in Figure 2.1 as red (A) and blue (B). Each atom on the lattice contributes one conduction electron.

Using the coordinates defined in Figure 2.1, the lattice vectors are defined, from the center of a honeycomb.

$$\vec{a}_1 = \frac{3a}{2}\hat{i} + \frac{\sqrt{3}a}{2}\hat{j} \quad (2.1)$$

$$\vec{a}_2 = \frac{3a}{2}\hat{i} - \frac{\sqrt{3}a}{2}\hat{j} \quad (2.2)$$

Here a is the carbon-carbon bond distance, 1.42 Å (CITE).

The reciprocal lattice vectors, \vec{b}_1 and \vec{b}_2 can now be found in the usual way.

CHAPTER 2. PROPERTIES OF CNTS

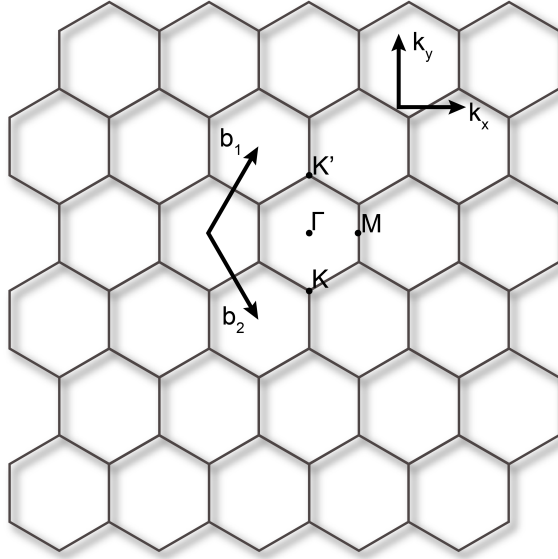


Figure 2.2: The reciprocal lattice of graphene. Vectors \vec{b}_1 and \vec{b}_2 define the Brillouin zone. The high symmetry points Γ , K , K' , and M are labeled.

$$a_i \cdot b_j = 2\pi\delta_{ij} \quad (2.3)$$

Here δ_{ij} is the Kronecker delta. The reciprocal lattice defined by \vec{b}_1 and \vec{b}_2 can be seen in Figure 2.2.

$$\vec{b}_1 = \frac{2\pi}{3a}\hat{i} + \frac{2\sqrt{3}\pi}{3a}\hat{j} \quad (2.4)$$

$$\vec{b}_2 = \frac{2\pi}{3a}\hat{i} - \frac{2\sqrt{3}\pi}{3a}\hat{j} \quad (2.5)$$

The reciprocal lattice is also a honeycomb lattice, rotated 90 degrees from the real space lattice. The size of each Brillouin zone is defined by the reciprocal lattice vectors above. A few high symmetry points have been labelled in the figure. Of particular note are the three K and three K' points. As will be seen in the band

CHAPTER 2. PROPERTIES OF CNTS

structure calculation, these are the points at which the conduction and valence bands will meet to form the Dirac cones that give rise to graphene's interesting low energy conduction properties.

2.1.2 Tight Binding Model

The simplest way to calculate the low energy electronic band structure for graphene is using a nearest neighbor tight binding model, also known as a linear combination of atomic orbitals (CITE). In this model, each conduction electron is tightly bound to a lattice site with a small probability of hopping only to a nearest neighbor site. With this simple picture for electron conduction, one can find the lowest energy bands in graphene.

Given that the model deals with the motion of individual electrons and their wavefunctions at each atomic site, the goal will be to solve the time independent Schrödinger equation.

$$\hat{H}\Psi = \varepsilon\Psi \quad (2.6)$$

Ψ is a single particle wavefunction over the whole graphene lattice. As such, it can be written as a linear combination of Bloch wavefucntions.

CHAPTER 2. PROPERTIES OF CNTS

$$u_A(\vec{r}) = \frac{1}{\sqrt{N}} \sum_{\vec{r}_A} e^{i\vec{k}\cdot\vec{r}_A} \phi_{2p_z}(\vec{r} - \vec{r}_A) \quad (2.7)$$

$$u_B(\vec{r}) = \frac{1}{\sqrt{N}} \sum_{\vec{r}_B} e^{i\vec{k}\cdot\vec{r}_B} \phi_{2p_z}(\vec{r} - \vec{r}_B) \quad (2.8)$$

These two functions represent Bloch waves localized on the A and B sublattices, respectively. With these definitions the full single-particle wavefunction can be rewritten as follows:

$$\Psi = C_A u_A + C_B u_B \quad (2.9)$$

$C_{A(B)}$ represents the amplitude of the wavefunction on the A(B) sublattice. With all of the above definitions the time independent Schrödinger equation can be rewritten in a matrix form:

$$\begin{pmatrix} H_{AA} & H_{AB} \\ H_{BA} & H_{BB} \end{pmatrix} \begin{pmatrix} C_A \\ C_B \end{pmatrix} = \varepsilon \begin{pmatrix} S_{AA} & S_{AB} \\ S_{BA} & S_{BB} \end{pmatrix} \begin{pmatrix} C_A \\ C_B \end{pmatrix} \quad (2.10)$$

Where:

$$H_{ij} = \langle u_i | H | u_j \rangle \quad (2.11)$$

$$S_{ij} = \langle u_i | u_j \rangle \quad (2.12)$$

For simplicity, the rest of this calculation will assume $\langle u_i | u_j \rangle = \delta_{ij}$. Meaning, there is no overlap of the two Bloch wavefunctions and that each of the wave functions is

CHAPTER 2. PROPERTIES OF CNTS

already properly normalized. Rewriting Equation 2.10 yields:

$$\begin{pmatrix} H_{AA} - \varepsilon & H_{AB} \\ H_{BA} & H_{BB} - \varepsilon \end{pmatrix} \begin{pmatrix} C_A \\ C_B \end{pmatrix} = 0 \quad (2.13)$$

Non-trivial solutions to Equation 2.13 exist only when:

$$\begin{vmatrix} H_{AA} - \varepsilon & H_{AB} \\ H_{BA} & H_{BB} - \varepsilon \end{vmatrix} = 0 \quad (2.14)$$

Solving equation 2.14 gives the energy eigenvalues in terms of the matrix elements defined in equation 2.11.

$$\varepsilon = H_{AA} \pm |H_{AB}| \quad (2.15)$$

Where the relations $H_{AA} = H_{BB}$ and $H_{AB} = H_{BA}^*$ were used.

In order to obtain a useful expression for the energy bands in terms of the electron momentum \vec{k} , Equation 2.15 must be simplified using the expressions for the Bloch wavefunctions.

$$H_{AA} = \frac{1}{N} \sum_{\vec{r}_A} \sum_{\vec{r}'_A} e^{i\vec{k} \cdot (\vec{r}_A - \vec{r}'_A)} \int \phi_{2p_z}^*(\vec{r} - \vec{r}_A) \hat{H} \phi_{2p_z}(\vec{r} - \vec{r}'_A) d^3\vec{r} \quad (2.16)$$

$$H_{AB} = \frac{1}{N} \sum_{\vec{r}_A} \sum_{\vec{r}_B} e^{i\vec{k} \cdot (\vec{r}_A - \vec{r}_B)} \int \phi_{2p_z}^*(\vec{r} - \vec{r}_A) \hat{H} \phi_{2p_z}(\vec{r} - \vec{r}_B) d^3\vec{r} \quad (2.17)$$

The summation in Equation 2.16 can be evaluated to yield:

CHAPTER 2. PROPERTIES OF CNTS

$$H_{AA} = \int \phi_{2p_z}^*(\vec{r} - \vec{r}_A) \hat{H} \phi_{2p_z}(\vec{r} - \vec{r}_A) d^3\vec{r} = \varepsilon_{p_z} \quad (2.18)$$

Where ε_{p_z} is the energy of a single electron on a p_z orbital. For the sake of simplicity, the rest of this chapter will assume $\varepsilon_{p_z} = 0$.

In order to simplify Equation 2.17 it is useful to define the vectors pointing from an atom on the B sublattice to its three nearest neighbors on the A sublattice.

$$\begin{aligned} \vec{\delta}_1 &= -a\hat{i} \\ \vec{\delta}_2 &= \frac{a}{2}\hat{i} - \frac{\sqrt{3}}{2}a\hat{j} \\ \vec{\delta}_3 &= \frac{a}{2}\hat{i} + \frac{\sqrt{3}}{2}a\hat{j} \end{aligned} \quad (2.19)$$

With these definitions Equation 2.17 can be rewritten as:

$$\hat{H}_{AB} = \sum_{i=1}^3 e^{i\vec{k}\cdot\vec{\delta}_i} \int \phi_{2p_z}^*(\vec{r}) \hat{H} \phi_{2p_z}(\vec{r} - \vec{\delta}_i) d^3\vec{r} \quad (2.20)$$

Since the exact form of the Hamiltonian is not known, the integral in Equation 2.20 cannot be evaluated. However, the integral clearly represents the overlap between the wavefunction of an electron in a p_z orbital on the A lattice and its nearest neighbor on the B lattice. With that in mind, the hopping amplitude t is defined:

$$t = \int \phi_{2p_z}^*(\vec{r}) \hat{H} \phi_{2p_z}(\vec{r} - \vec{\delta}_i) d^3\vec{r} \quad (2.21)$$

CHAPTER 2. PROPERTIES OF CNTS

Note, there is only one hopping amplitude, independent of the index i , since the distance between all nearest neighbors, $|\delta_i|$, is the same. With this definition, the overlap integral can be rewritten once more.

$$H_{AB} = t \sum_{i=1}^3 e^{i\vec{k} \cdot \vec{\delta}_i} \quad (2.22)$$

Equation 2.22 can be combined with the assumption that the onsite energy can be set to zero, $\varepsilon_{p_z} = 0$ to give the final effective Hamiltonian for this model.

$$\hat{H} = \begin{pmatrix} 0 & t \sum_i e^{i\vec{k} \cdot \vec{\delta}_i} \\ t \sum_i e^{-i\vec{k} \cdot \vec{\delta}_i} & 0 \end{pmatrix} \quad (2.23)$$

Using these same results in Equation 2.15 gives the two lowest energy bands in terms of the hopping amplitude, t .

$$\varepsilon(\vec{k}) = \pm t \left| \sum_i e^{i\vec{k} \cdot \vec{\delta}_i} \right| \quad (2.24)$$

$$\varepsilon(\vec{k}) = \pm t \sqrt{1 + 4 \cos\left(\frac{3a}{2}k_x\right) \cos\left(\frac{\sqrt{3}a}{2}k_y\right) + 4 \cos^2\left(\frac{\sqrt{3}a}{2}k_y\right)} \quad (2.25)$$

These two bands can be seen in Figure 2.3. Note that the plot does not assume $S_{ij} = \langle u_i | u_j \rangle = \delta_{ij}$, which introduces some asymmetry in the valence and conduction bands.

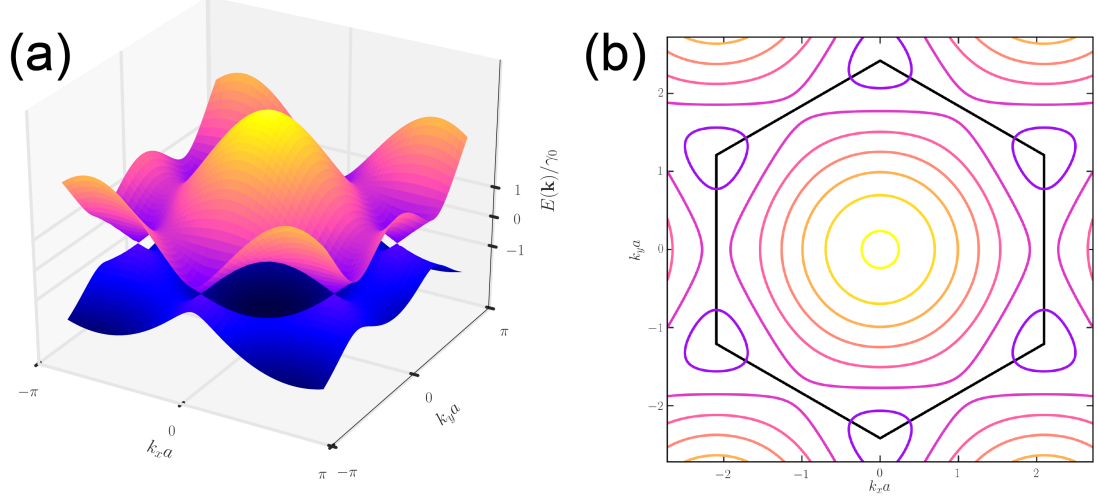


Figure 2.3: (a) The π -bands of graphene calculated using a nearest neighbor tight binding model. (b) A contour plot of the upper band with the first Brillouin zone drawn. The bands meet at the three K and three K' points at the vertices of the Brillouin zone.

2.1.3 Low Energy Bandstructure of Graphene

For low energy electronic excitations, conduction will be dominated by the band-structure near the K and K' points. There are only two inequivalent points, since the other 4 are equivalent by the symmetry of the honeycomb lattice. Consider the two points located at:

$$\vec{K} = 0\hat{i} - \frac{4\pi}{3\sqrt{3}a}\hat{j} \quad (2.26)$$

$$\vec{K}' = -\vec{K} = 0\hat{i} + \frac{4\pi}{3\sqrt{3}a}\hat{j} \quad (2.27)$$

To get the low-energy dispersion relation, expand the Hamiltonian in Equation 2.23 around the K point.

$$\vec{k} = \vec{K} + \vec{q} \quad (2.28)$$

$$\hat{H} \approx -i\frac{3at}{2} \begin{pmatrix} 0 & q_x + iq_y \\ -(q_x - iq_y) & 0 \end{pmatrix} \quad (2.29)$$

Similarly, expanding around the K' point yields:

$$\hat{H} \approx -i\frac{3at}{2} \begin{pmatrix} 0 & q_x - iq_y \\ -(q_x + iq_y) & 0 \end{pmatrix} \quad (2.30)$$

By defining $v_f \equiv 3at/2\hbar$, using the standard Pauli matrices, and rotating the phase, Equations 2.29 and 2.30 can be written in a more suggestive form.

$$\hat{H}_K = \hbar v_f \vec{\sigma} \cdot \vec{q} \quad (2.31)$$

$$\hat{H}_{K'} = \hbar v_f \vec{\sigma}^* \cdot \vec{q}$$

These Hamiltonians describe massless Dirac fermions in 2D. This is clear in the low-energy dispersion relation.

$$\varepsilon(\vec{q}) = \pm \hbar v_f q \quad (2.32)$$

It is also important to note, in Equation 2.31, that the sublattice structure has lead to a spin-1/2 degree of freedom. This degree of freedom is known as the valley degeneracy or pseudospin.

CHAPTER 2. PROPERTIES OF CNTS

A useful consequence of the pseudospin is the reduction in scattering in graphene and carbon nanotubes. The reduced backscattering is a result of the introduction of an additional symmetry to the system. This reduction in scattering leads to unusually high mobilities and long spin coherence lengths in both materials. The increased spin coherence length is exactly what lead to the choice of carbon nanotubes for this work.

2.2 Electronic Bandstructure of Carbon Nanotubes

Now that the bandstructure a graphene sheet has been calculated, finding the electronic bandstructure of various carbon nanotubes is as simple as applying a few boundary conditions.

The structure of a carbon nanotube can be completely described by its chiral vector.

$$\vec{C}_h = m\vec{a}_1 + n\vec{a}_2 \quad (2.33)$$

$$\vec{C}_h = \frac{3}{2}(n+m)a\hat{i} + \frac{\sqrt{3}}{2}(n-m)a\hat{j}$$

This vector describes how to roll a graphene sheet to form the nanotube. The tube is formed by rolling the graphene sheet such that the tip and tail of \vec{C}_h meet. The indices (n, m) describe the type of nanotube that is formed. A tube where $0 < m < n$

CHAPTER 2. PROPERTIES OF CNTS

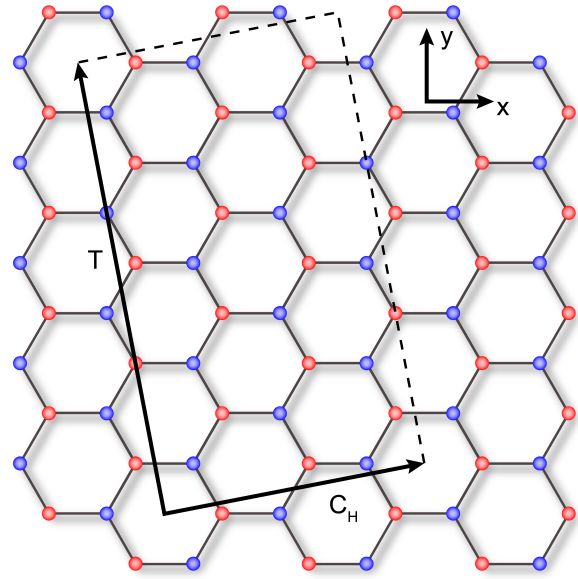


Figure 2.4: The real-space structure of a carbon nanotube. The nanotube unit cell is defined by the vectors \vec{C}_h and \vec{T}

is known as chiral, $m = n$ is an armchair nanotube, and $m = 0$ is a zig-zag nanotube. Armchair and zig-zag tubes get their names from the shape of the carbon bonds on the edge of the unit cell.

An example of a chiral (2,1) nanotube unit cell can be seen in Figure 2.4. The unit cell is defined by the chiral vector \vec{C}_h and the translation vector T . Which is defined as:

$$\vec{T} = t_1 \vec{a}_1 + t_2 \vec{a}_2 \quad (2.34)$$

where $t_1 = (2m + n)/d_R$, $t_2 = (2n - m)/d_R$ and $d_R = \gcd(2n + m, 2m + n)$. These two vectors can be used to calculate a few basic properties of the nanotube. The diameter of the nanotube is found from the chiral vector.

CHAPTER 2. PROPERTIES OF CNTS

$$d = \left| \vec{C}_h \right| / \pi = \frac{\sqrt{3}a}{\pi} \sqrt{n^2 + nm + m^2} \quad (2.35)$$

The number of graphene unit cells contained in the nanotube unit cell is also easily calculated.

$$N = \frac{\left| \vec{C}_h \times \vec{T} \right|}{\left| \vec{a}_1 \times \vec{a}_2 \right|} = \frac{2}{d_R} \sqrt{n^2 + nm + m^2} \quad (2.36)$$

Knowing the number of graphene unit cells contained in the nanotube unit cell yields a lot of useful information about the band structure. There are $2N$ carbon atoms in the nanotube unit cell and N conduction electrons. There will be $2N$ bands (one for each carbon atom) that will be half-filled, just like the graphene bandstructure.

The reciprocal lattice vectors for the carbon nanotube defined by (n, m) can be found in the usual way.

$$\begin{aligned} \vec{C}_h \cdot \vec{K}_1 &= \vec{T} \cdot \vec{K}_2 = 2\pi \\ \vec{C}_h \cdot \vec{K}_2 &= \vec{T} \cdot \vec{K}_1 = 0 \end{aligned} \quad (2.37)$$

$$\begin{aligned} \vec{K}_1 &= -\frac{(t_2 \vec{b}_1 - t_1 \vec{b}_2)}{N} \\ \vec{K}_2 &= \frac{(m \vec{b}_1 - n \vec{b}_2)}{N} \end{aligned} \quad (2.38)$$

The reciprocal space of the unrolled nanotube is quantized along \vec{K}_1 and continuous along \vec{K}_2 . This means the electron momentum k in the nanotube is quantized

CHAPTER 2. PROPERTIES OF CNTS

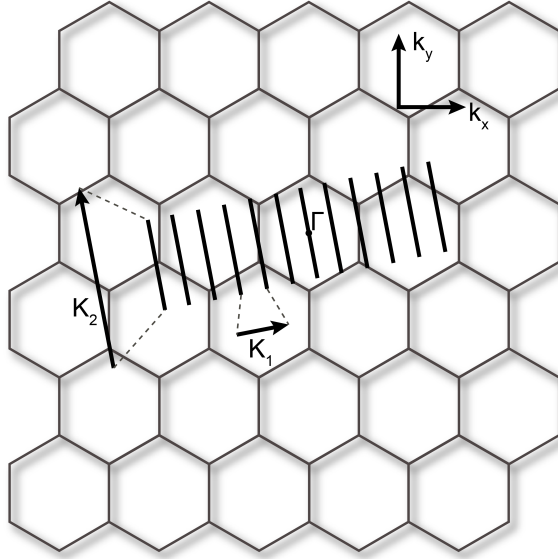


Figure 2.5: The reciprocal lattice of a carbon nanotube, defined by the vectors K_1 and K_2

along the direction of C_h . These quantized 'cutting lines' define the electronic bands in the carbon nanotube.

$$\vec{k} \cdot \vec{C}_h = 2\pi\mu \quad (2.39)$$

Where μ is an integer from $1 - N/2$ to $N/2$ and $\mu = 0$ cuts through the Γ point at the center of the graphene Brillouin zone. The structure of the nanotube reciprocal lattice, defined by K_1 and K_2 can be seen in Figure 2.5.

With all of these definitions, the electron momentum in the carbon nanotube can be rewritten.

$$\vec{k} = \mu \vec{K}_1 + k_{\parallel} \frac{\vec{K}_2}{|\vec{K}_2|} \quad (2.40)$$

CHAPTER 2. PROPERTIES OF CNTS

The bands for a generic nanotube can be found by simply inserting this definition for the momentum into the graphene bands derived in Equation 2.25.

2.2.1 Types of Carbon Nanotubes

The electronic properties of a carbon nanotube are determined by its chirality, (n, m) . If one of the cutting lines, as seen in Figure 2.5, passes through a K or K' point, the nanotube will have a metallic band structure. Like in graphene, two of the valence and conduction bands will meet at discrete points at the Fermi energy. If this is not the case, and none of the cutting lines pass through a K or K' point, the nanotube will be semiconducting with a bandgap determined by the chirality.

To determine if a nanotube is semiconducting or metallic, one can look at the projection of \vec{K} , the vector pointing to a K point in the graphene Brillouin zone, and \vec{K}_1 , the nanotube reciprocal lattice vector.

$$\frac{\vec{K} \cdot \vec{K}_1}{\vec{K}_1 \vec{K}_1} = \frac{(2n + m)}{3} \quad (2.41)$$

From Equation 2.41, it is clear that a nanotube is metallic if $(n - m) \bmod 3 = 0$. There are two other cases, where $(n - m) \bmod 3 = 1$ or $(n - m) \bmod 3 = 2$. Each of these results in a semiconducting nanotube. Based on these results, in a collection of nanotubes with random chirality, (n, m) , there will be roughly 1/3 metallic and 2/3 semiconducting nanotubes.

Figure 2.6 shows the full bandstructure of a metallic $(5, 5)$ armchair nanotube and

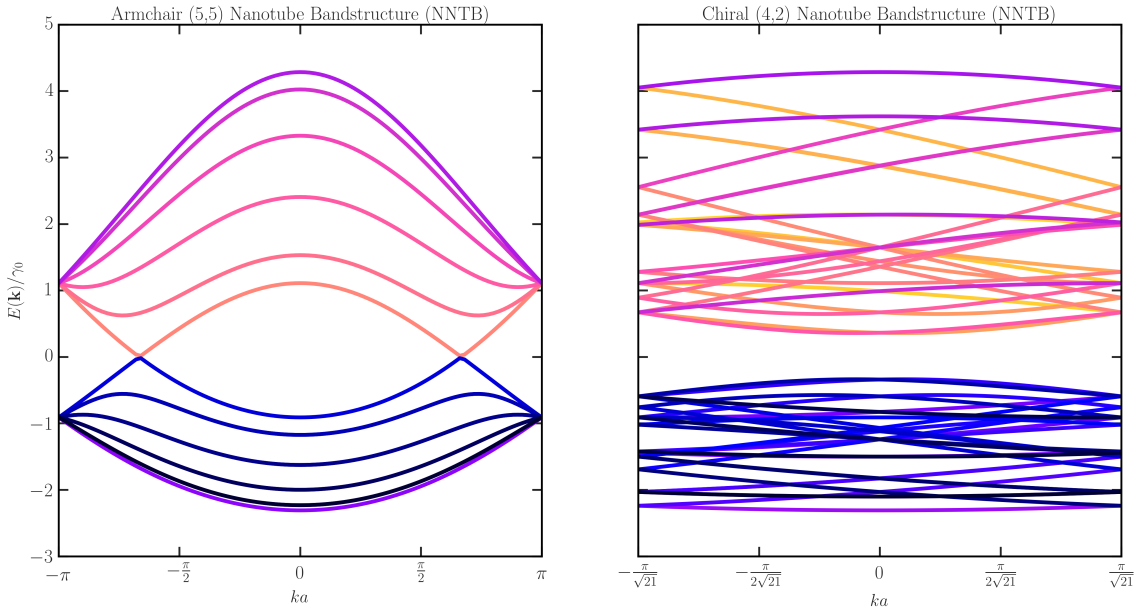


Figure 2.6: Two types of carbon nanotube bandstructure. The left plot shows a metallic $(5, 5)$ armchair nanotube. The right plot shows a semiconducting $(4, 2)$ chiral nanotube.

a semiconducting $(4, 2)$ chiral nanotube. These have 20 and 56 bands, respectively.

2.2.2 Low Energy Bandstructure of Carbon Nanotubes

To calculate the full set of bands for a generic nanotube (n, m) is cumbersome. The basic properties for a generic nanotube can be more easily calculated by first expanding the graphene bands about the K and K' points as in Equation 2.32, then using the quantized momentum derived in Equation 2.40. Doing this yields the low energy dispersion relation for a generic carbon nanotube.

CHAPTER 2. PROPERTIES OF CNTS

$$\varepsilon_\mu(k) = \pm \frac{2\hbar v_f}{d} \sqrt{\left(\frac{m-n}{3} - \mu\right)^2 + \left(\frac{kd}{2}\right)^2} \quad (2.42)$$

Where μ is the band index, d is the nanotube diameter, and k is the electron momentum along the nanotube axis. Looking at the first term in parentheses, it is clear that the nanotube will be metallic if $(m - n)/3$ is an integer. In that case, there will be some integer μ for which the valence and conduction bands meet at the Fermi energy. This is consistent with the condition derived previously for metallic and semiconducting chiral vectors. Using that information the low energy bandstructure can be written a little more suggestively.

$$\varepsilon(k) = \pm \left(\frac{1}{2} E_g(n, m) + \frac{\hbar^2}{2m^*} k^2 \right) \quad (2.43)$$

$$\varepsilon(k) = \pm \hbar v_f k \quad (2.44)$$

These are the approximate bandstructures at low energy. Semiconducting nanotubes have a bandgap, $E_g(n, m)$ dependent on the chirality, and an effective mass m^* dependent on the lowest band curvature. Metallic nanotubes maintain the massless Dirac fermion properties found in graphene at low energies.

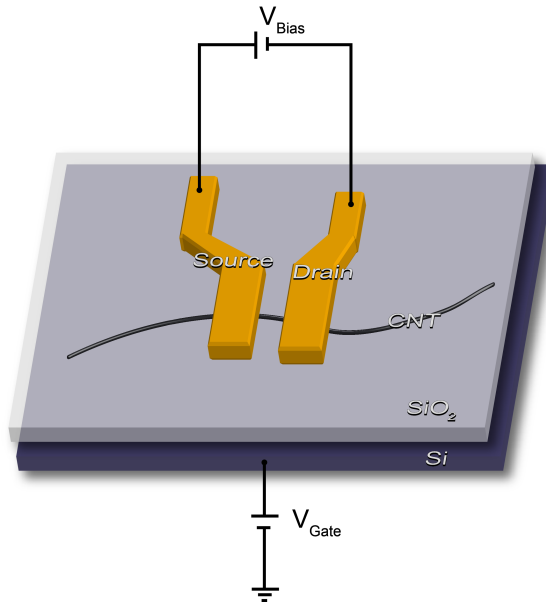


Figure 2.7: Schematic of a carbon nanotube field effect transistor.

2.3 Carbon Nanotube Field Effect Transistors

Now that the electronic bandstructure of a carbon nanotube is known, we can move on to discussing electric measurements on simple carbon nanotube devices. At room temperature, the simplest device that one can make with a carbon nanotube is a field effect transistor. A nanotube is placed, or grown, on a silicon substrate capped with an insulating silicon dioxide layer. Source and drain contacts are then made to the nanotube. The completed three terminal device is made up of the source, drain, and silicon substrate acting as the gate, with the silicon dioxide layer serving as the gate dielectric. A schematic of such a device is seen in Figure 2.7

CHAPTER 2. PROPERTIES OF CNTS

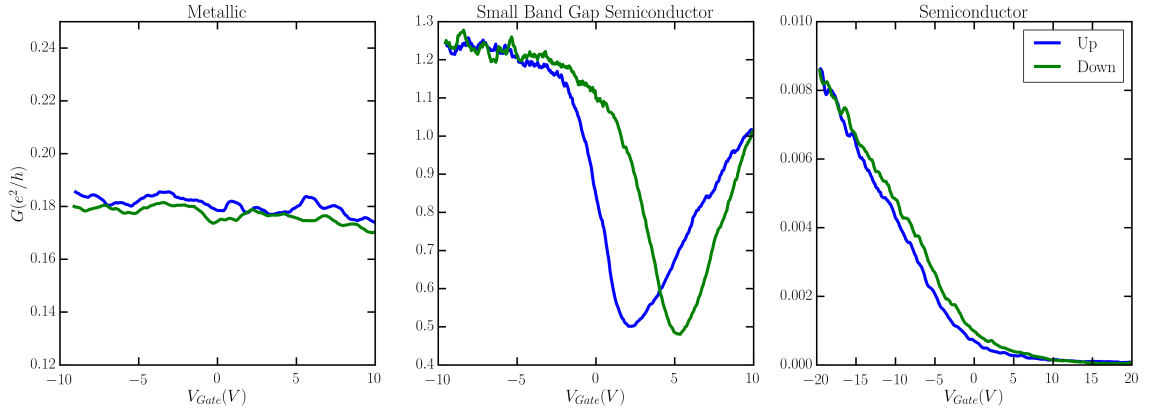


Figure 2.8: Current versus gate voltage characteristics for three types of CNTFET.

Measurements on carbon nanotube field effect transistors (CNTFETs) depend on the type of carbon nanotube that has been contacted.

Metallic source/drain contacts typically form Schottky barriers with carbon nanotubes. The polarity of the resulting CNTFET is thus determined by the relation between the work function of the contact material and nanotube. For metals with a relatively high work function, such as Pd, Ti, Cr, and Co, the devices are expected to be p-type. Metals with a lower work function, such as Al, Mg, and Sc, can produce n-type transistors. However, many of these low work function metals also happen to have a very poor wettability on the nanotube surface, which leads to large contact resistances, making the devices very difficult to fabricate and measure.

CHAPTER 2. PROPERTIES OF CNTS

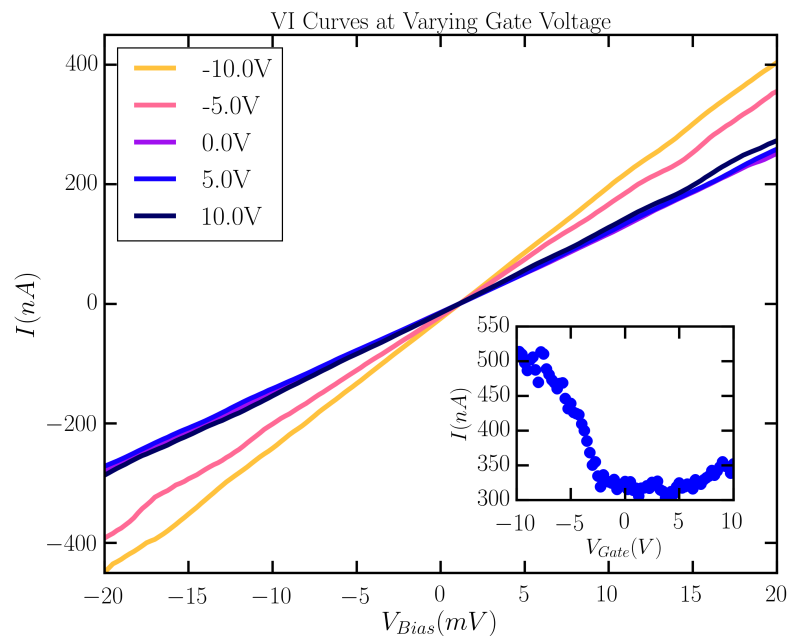


Figure 2.9: IV characteristics of a typical small band gap semiconducting CNTFET. The current saturates at higher bias voltage, but is not typically measured due to avalanche breakdown of the devices. Inset: Current versus gate at a fixed bias for the same device.

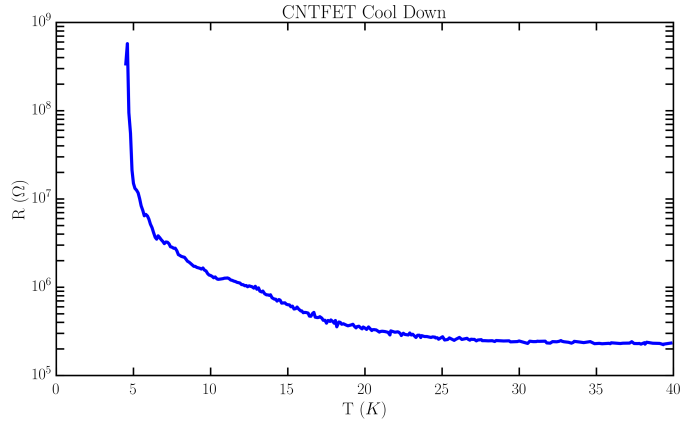


Figure 2.10: R-T curve of a CNTFET cooled to 4 K

2.4 Carbon Nanotube Quantum Dots

When cooled to low temperatures ($\lesssim 10$ K), the device drawn in Figure 2.7 exhibits quantum mechanical behavior. For a sufficiently short channel length ($L \lesssim 500$ nm), electrons become confined within the carbon nanotube and behave like quantum mechanical particles in a box. This device is called a quantum dot. The resistance versus temperature plot in Figure 2.10 shows the sharp increase in resistance as the tunneling through the device is suppressed at low temperatures.

Once the device is cold, the filling of electrons can be controlled by varying the bias and gate voltages. A schematic of the relevant energies is seen in Figure 2.11. The bias voltage can be used to change the relative chemical potential of the source and drain metals. The gate voltage is then used to change the chemical potential on the quantum dot relative to the source/drain.

The model we will use to discuss this device is called the constant interaction

CHAPTER 2. PROPERTIES OF CNTS

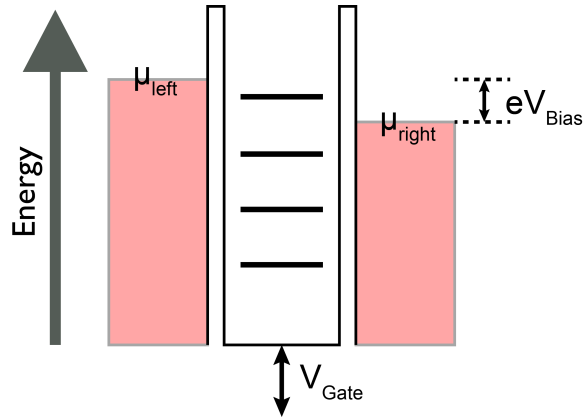


Figure 2.11: Quantum dot energy diagram.

model. Tunnel barriers naturally form at the interface between the metal contacts and the nanotube. At low temperatures this leads to weak tunneling on/off the nanotube (quantum dot). Because of this, the number of electrons confined on the dot at any given time is an integer, N . Adding an additional electron to the dot requires overcoming the Coulomb repulsion between the additional electron and those already confined on the dot. The constant interaction model treats this charging energy as a constant, regardless of the number of electrons confined on the dot. The model also assumes that the states on the quantum dot are not affected by the electron-electron interactions.

With these assumptions, it is simple to find the energy required to add an electron to the dot. To begin, the total energy on the dot can be approximated.

$$U(N) = \frac{[e(N - N_0) - C_g V_g]^2}{2C} + \sum_N E_n \quad (2.45)$$

CHAPTER 2. PROPERTIES OF CNTS

Here N_0 is the charge on the dot at zero gate voltage, C_g is the gate capacitance, and $C = C_{source} + C_{drain} + C_{gate}$. The summation represents the sum over all of the filled quantum dot levels, denoted by E_n . The chemical potential is defined as $\mu(N) = U(N) - U(N+1)$.

$$\mu(N) = \left(N - N_0 - \frac{1}{2} \right) \frac{e^2}{2C} - \frac{eC_g V_g}{C} + E_N \quad (2.46)$$

Finally, the addition energy is given by the change in chemical potential from the N to $N+1$ levels.

$$\begin{aligned} \Delta\mu(N) &= \frac{e^2}{2C} + (E_{N+1} - E_N) \\ \Delta\mu(N) &= \frac{e^2}{2C} + \Delta E \end{aligned} \quad (2.47)$$

Equation 2.47 gives the amount of energy required to add the N th electron to the quantum dot. Note that the first term in this energy is the constant interaction term representing the Coulomb repulsion, $E_{charging} = \frac{e^2}{2C}$.

The simplest measurement to make on a quantum dot like the one described here, is to measure the conductance as a function of the gate voltage. Figure 2.12 shows diagrammatically how the process works. At very small bias ($\mu_{left} \sim \mu_{right}$), the gate voltage is varied. When the chemical potential on the source/drain are resonant with a level on the quantum dot, a peak is observed in the conductance. Otherwise, conductance across the dot is suppressed. Spacing between conductance peaks should

CHAPTER 2. PROPERTIES OF CNTS

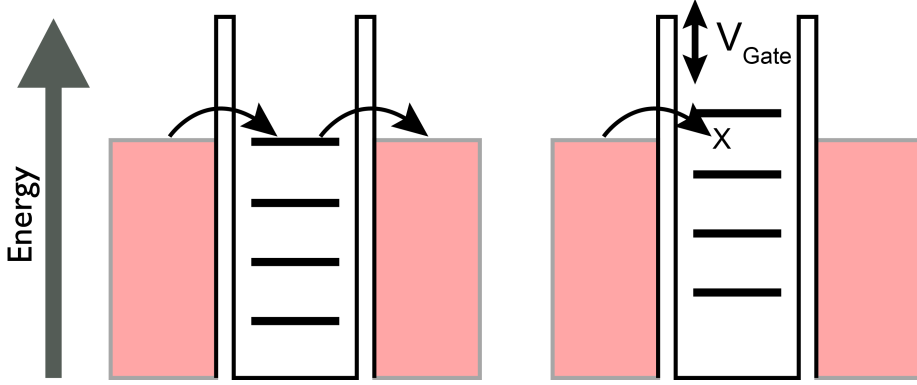


Figure 2.12: Left: A quantum dot level resonant with the source/drain chemical potential. Right: The same device in the blockaded region.

follow Equation 2.47.

Figure 2.13 shows conductance as a function of gate voltage through an actual carbon nanotube quantum dot device. A close look at the spacing of the conductance peaks reveals some hints of four-fold symmetry that is an important part of the structure of the nanotube quantum dot. Adding the first electron to the dot costs an energy $\Delta\mu(N) = \frac{e^2}{2C} + \Delta E$. However, the electron spin and valley degeneracy combine to give each level in the quantum potential well a degeneracy of four. The next three electrons added move into the same level, which only requires an energy of $\Delta\mu(N) = \frac{e^2}{2C}$ for each electron. This pattern continues for each level on the dot, such that the energy required to add the N electron is always larger than the energy required to add the $N + 1$, $N + 2$, and $N + 3$ electrons.

Varying the bias voltage leads to similar behavior, as illustrated in Figure 2.14. If a level on the quantum dot lies between the source and drain chemical potentials, conductance is possible. Otherwise, if no level lies in that window, the device is again

CHAPTER 2. PROPERTIES OF CNTS

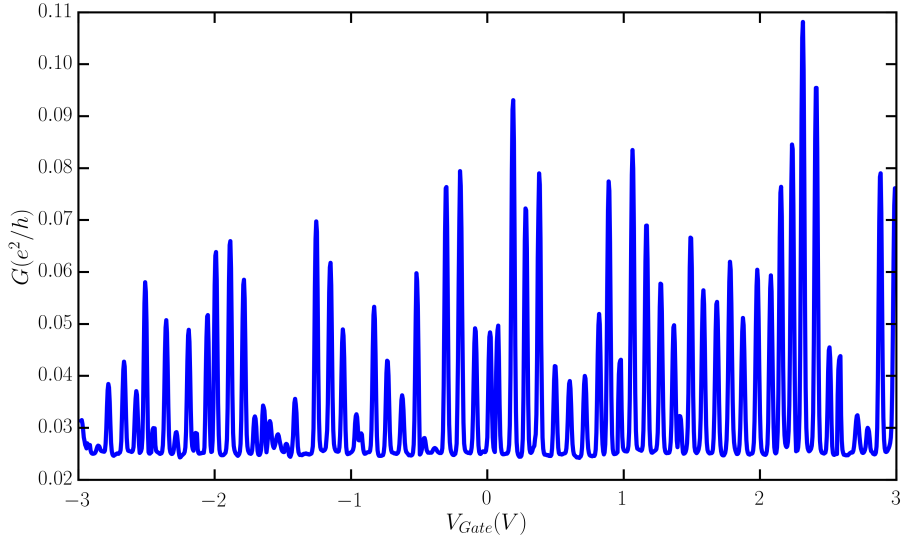


Figure 2.13: Conductance as a function of applied gate voltage in a cobalt contacted nanotube quantum dot.

in the blockaded regime. With further increases of the bias voltage, higher order conductance processes are possible.

Figure 2.15 shows current and conductance as a function of applied bias voltage. It is clear from the differential conductance plot, for low bias voltages the conductance is suppressed across the dot. At higher bias, a quantum dot level moves into the bias window and conductance increases. Increasing the bias further from there allows for transport through excited states and higher order processes, which will be discussed further in later chapters.

Finally, measuring conductance as a function of both the bias and gate produces a stability diagram of the quantum dot. An example of this can be seen in Figure 2.16. Looking at a cut of this plot at constant bias reproduces Figure 2.13. Similarly, a cut at constant gate voltage reproduces Figure 2.15. Putting both together produces

CHAPTER 2. PROPERTIES OF CNTS

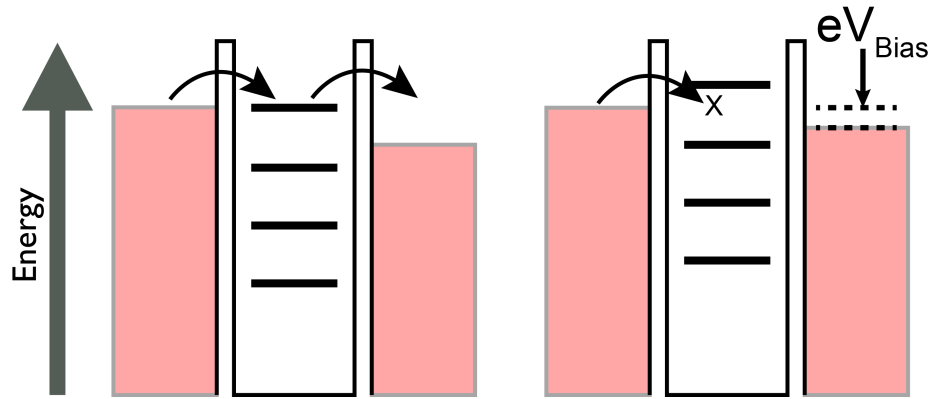


Figure 2.14: Left: A quantum dot level resonant with the drain chemical potential. Right: The same device in the blockaded region.

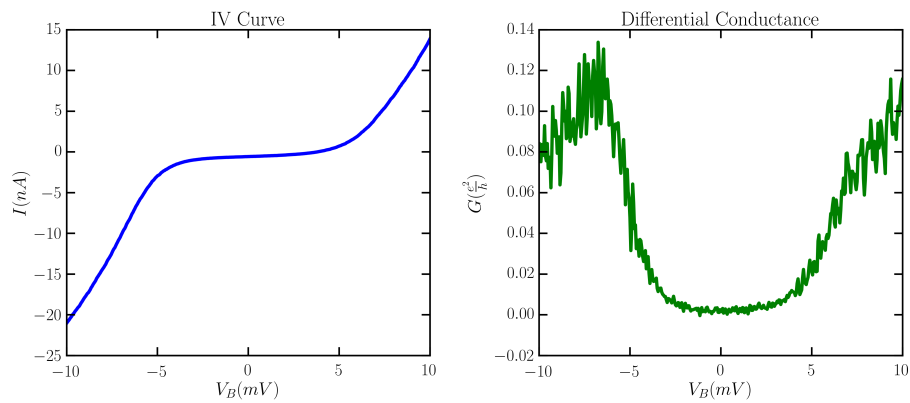


Figure 2.15: Left: An IV curve at fixed gate voltage Right: Differential conductance measured at fixed gate voltage.

CHAPTER 2. PROPERTIES OF CNTS

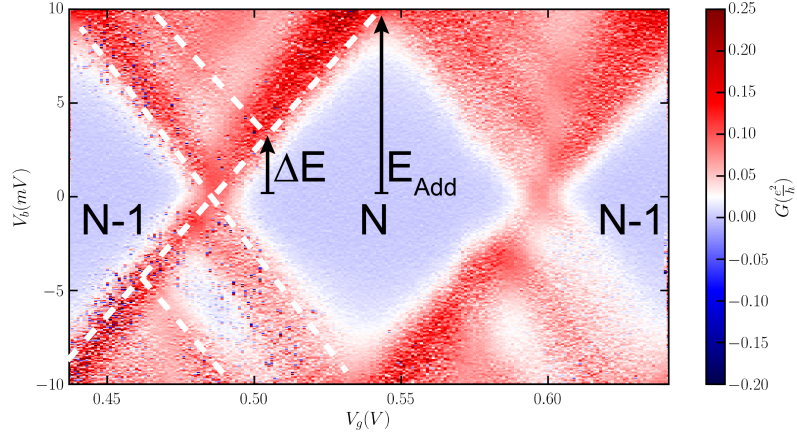


Figure 2.16: Conductance of a cobalt contacted nanotube quantum dot at 4K as a function of bias and gate voltages.

diamond-shaped regions in which the charge on the quantum dot is constant, denoted by $N - 1$, N , and $N + 1$ in the figure. The white dashed lines serve as a guide to the eye. The two black arrows mark the level spacing, ΔE , and addition energy E_{Add} (or $\Delta\mu$). By measuring both of these quantities it is possible to know the level spacing on the quantum dot and the capacitance of the device. By observing changes in the conductance peaks at different fillings and applied fields much can be learned about the levels on, interactions in, and transport across the quantum dot.

Chapter 3

Carbon Nanotube Growth and Placement

There are several methods that can be used to deposit nanotubes onto a substrate. Two of these methods, random dispersion and catalyst island growth, are discussed here. Additional methods, such as stamping [1,2], were not utilized for this work and will not be discussed.

3.1 Random Dispersion

The oldest, and least reliable, method of nanotube device fabrication, is what will be referred to as random dispersion. First, nanotubes are grown in bulk through chemical vapor deposition (or other preferred method). Then, the nanotubes are

CHAPTER 3. GROWTH AND PLACEMENT

Table 3.1: Powder Catalyst

Fe(NO ₃) ₃ · 9 H ₂ O	20 mg
MoO ₂ (acac) ₂	5 mg
Al ₂ O ₃	15 mg

suspended in a solution. Finally, the nanotubes are cast onto a substrate. Nanotubes can then be located relative to some predefined markers on the substrate.

3.1.1 Catalyst

All of the devices discussed in this thesis have utilized the same, iron-based catalyst [3,4]. The simplest way to create this catalyst is to combine the ingredients in Table 3.1 in a mortar and pestle and grind until it turns a uniform dark orange color. Adding some additional alumina seems to promote growth of longer tubes, possibly by lowering the density of tubes grown from each alumina/iron/molybdenum particle.

3.1.2 Growth

Of the many possible techniques for nanotube growth, we choose chemical vapor deposition for its simple implementation. The process is carried out in a Lindberg Blue tube furnace using a 1 inch diameter quartz tube. The furnace, quartz tube, and exhaust filtering are seen in Figure 3.1. Despite its poor looks, this setup has been repeatedly, and successfully, leak checked. Oxygen leaks can be detrimental to

CHAPTER 3. GROWTH AND PLACEMENT

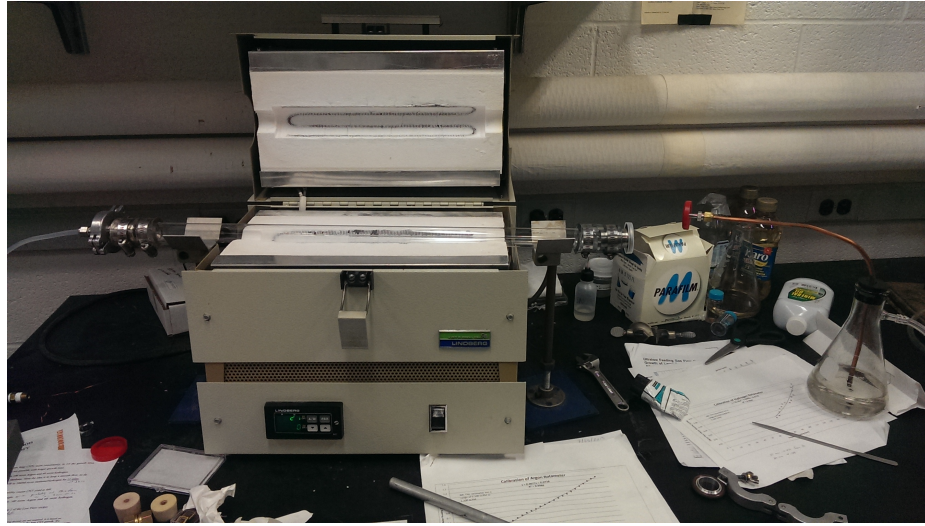


Figure 3.1: The tube furnace fitted with a 1" diameter quartz tube. The tube is sealed at both ends using 1" rubber tubing, cable clamps, and KF25 fittings. Gas flows from left to right in the picture. The gas flows out of the furnace into a mineral oil bubbler to keep hot hydrogen from reaching the air in the room. Gas then flows from the bubbler into the building exhaust.

the nanotube growth process by forming CO and CO₂ with any free carbon.

The gases used in the CVD process, argon, hydrogen, and methane, are fed into the furnace using a custom-made gas handling panel. This was originally constructed by Matt Oresky, a JHU undergraduate working in our lab with post-doc Atikur Rahman. The panel has three gas channels, each with its own analog flowmeter, needle valve, and on/off valve. A digital flowmeter placed at the right side of the panel reads the total flow of combined gas exiting the panel to the furnace. The gas handling panel can be seen in Figure 3.2

The growth procedure begins with filling a ceramic crucible with the iron catalyst described in 3.1.1. The catalyst should be spread in a thin layer across the bottom of the crucible, which is then loaded into the center of a 2-4 foot long quartz tube.

CHAPTER 3. GROWTH AND PLACEMENT

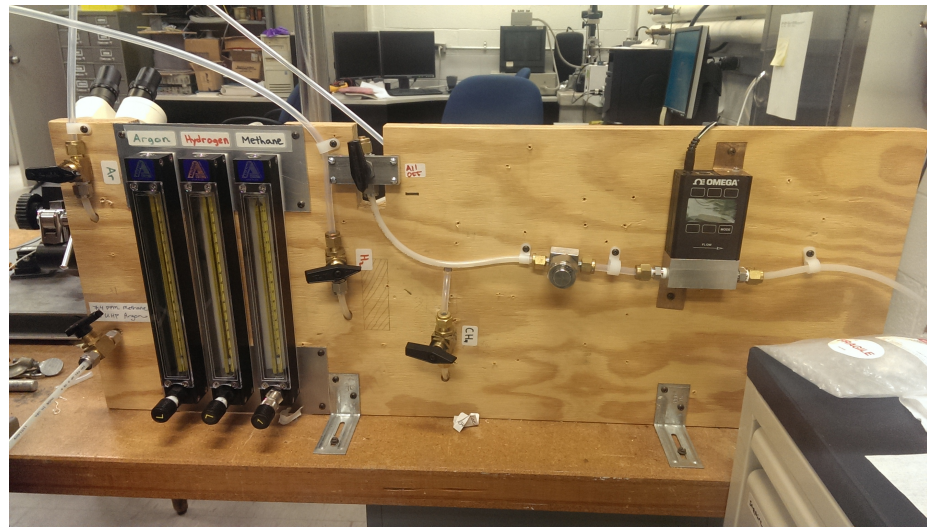


Figure 3.2: The gas handling panel for our Lindberg tube furnace. Gas flow is from left to right.

The tube is sealed at each end, one side connected to the gas handling panel, and the other connected to the mineral oil filter and building exhaust. Our standard nanotube growth recipe is as follows:

1. Purge the tube by flowing 2000 sccm of Ar for 20 minutes
2. Heat tube to 1000 °C while flowing 1000 sccm Ar and 200 sccm H₂
3. Flow 2000 sccm CH₄ and 200 sccm H₂ for 10 minutes.
4. Set temperature to 0 °C and let the furnace cool while flowing 1000 sccm Ar and 200 sccm H₂

The actual nanotube growth occurs during the methane flow step. The 200 sccm H₂ flow can be omitted, but it does seem to help promote nanotube growth. The flow rates do not need to be precise. Most nanotubes grow in the first few seconds of

CHAPTER 3. GROWTH AND PLACEMENT

methane flow regardless of the flow rate. The Ar and H₂ are simply to keep O₂ and H₂O out of the tube.

3.1.3 Nanotube Placement

After the CVD process, the nanotubes remain attached to the iron/alumina/molybdenum catalyst particles, which must be removed before depositing onto a silicon substrate. The nanotube/catalyst powder is first scraped from the ceramic crucible used in the tube furnace. The powder is then mixed with either dichloroethane or dichlorobenzene in a 1 mg to 10 mL ratio. Dichlorobenzene has been found to leave less residue after deposition, but may promote more damage to nanotubes during sonication. Some attempts were made to use water along with the surfactant SDS. However, SDS turned out to be difficult to remove and no devices were made in this way.

To remove the catalyst particles from the nanotubes, the solution described above must be placed in an ultrasonic bath for 1-60 minutes. The amount of time needed varied a great deal depending on the equipment and solvent used. The goal of this step is to break up large pieces of catalyst, separate nanotube bundles, and break individual nanotubes away from their catalyst particles. Sonication can be stopped when no large pieces of catalyst/nanotube material are visible and the solution has a uniform black color. Leaving the solution in the sonicator for too much time will begin to break long nanotubes.

CHAPTER 3. GROWTH AND PLACEMENT

When sonication is complete, the solution is transferred to a centrifuge. This step is intended to precipitate the loose catalyst particles from the solution, while leaving the much lighter nanotubes suspended. The centrifuge used in our lab runs at 2200 rpm and nanotube solutions are left inside for 5-10 minutes. Once the centrifuge stops, the precipitate is discarded and the supernate, containing the suspended nanotubes, is reserved. We also tested using a high-speed, air-powered centrifuge running at 100 000 rpm to separate nanotubes and catalyst. This did lead to much better catalyst separation and cleaner results.,,

Now the solution is ready for deposition on a silicon substrate. The substrates are typically pre-patterned with a set of reference markers placed by optical (A.1.2) or electron beam lithography (A.3). An example of a patterned substrate can be seen in Figure 3.3

3.1.4 Conclusion

Despite having some success fabricating devices using randomly dispersed nanotubes and EFM scans, the process was found to be too unreliable for frequent use. The main failure point was the preparation of nanotube solutions after growth. The concentrations varied significantly, often producing samples with dense nanotube coverage or no nanotubes found in the regions imaged. Additionally, the process of making a suspended nanotube solution is time consuming. Even those solutions with a useful concentration of nanotubes only remain fully suspended for less than 1 hour.

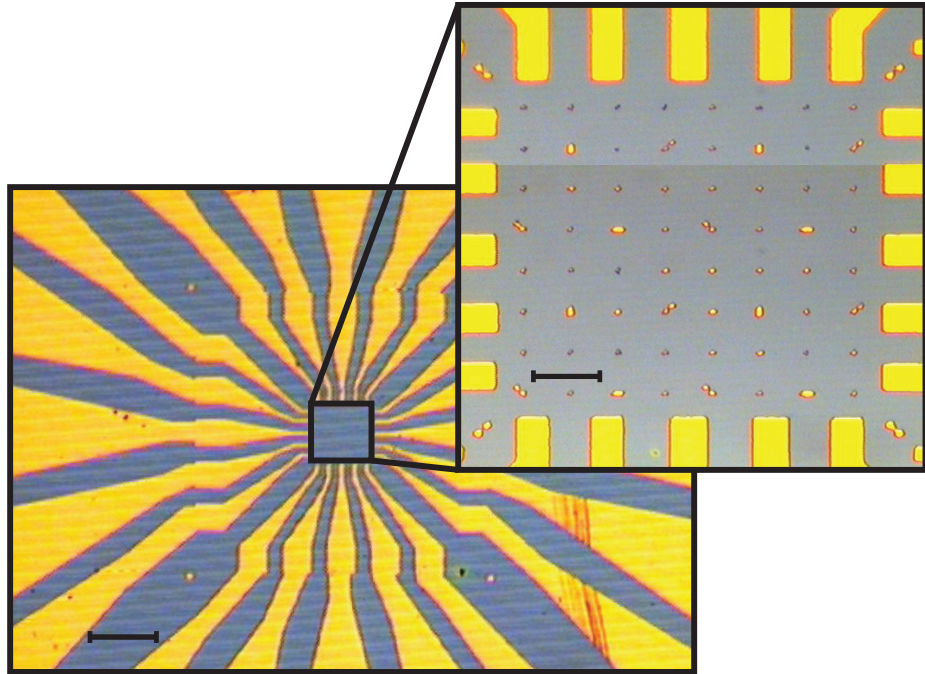


Figure 3.3: A Si/SiO₂ substrate with 1 μm Au markers. Left scale bar: 100 μm . Right scale bar: 20 μm

3.2 Catalyst Island Growth

In 1998 [4], it was discovered that the same type of catalyst used to grow nanotubes in powder form (Section 3.1.1), could be suspended in solution, patterned, and used to grow nanotubes directly on silicon substrates. When paired with high melting point metals and optical lithography, nanotubes can be grown directly on patterned substrates in known locations. Devices prepared this way take just a fraction of the time to produce.

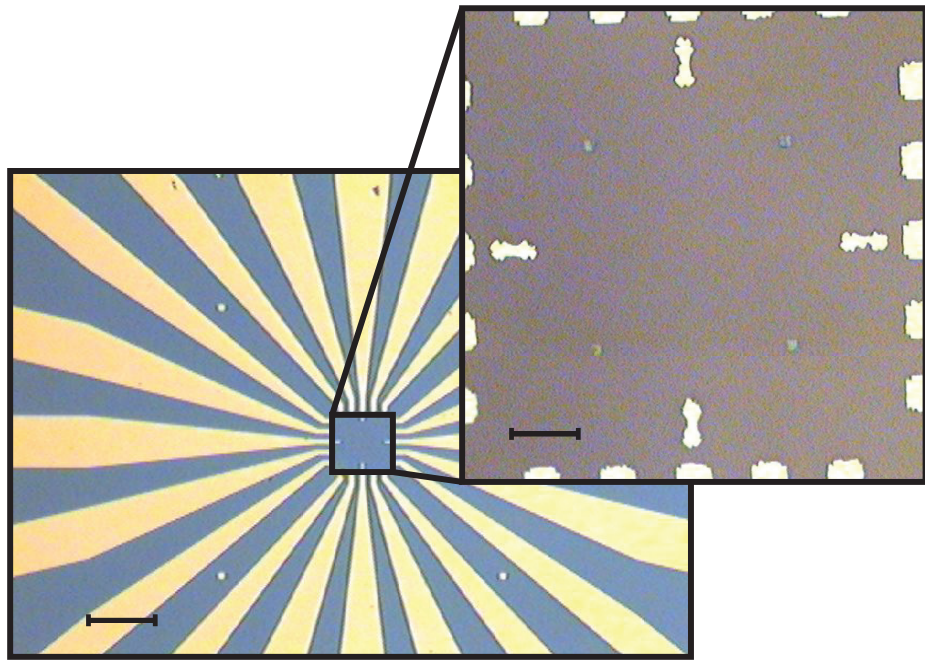


Figure 3.4: A Si/SiO₂ substrate with 3 μm catalyst islands and Mo leads. Left scale bar: 100 μm. Right scale bar: 20 μm

3.2.1 Catalyst

Many different types of catalyst particles can be used in the growth of carbon nanotubes. The ideal catalyst for patterned growth must be compatible with electron beam or optical lithography. Table 3.2 lists most of the catalysts tested in the Markovic lab. To test each catalyst, sputtered molybdenum leads were patterned using the mask aligner and Futurex NR9 resist. Catalyst islands were then patterned using electron beam lithography. Figure 3.4 shows an example of a substrate with Mo leads and catalyst islands.

All of the devices discussed in this thesis were produced using the Fe/Mo/alumina catalyst suspended in water. The islands were patterned using electron beam lithog-

CHAPTER 3. GROWTH AND PLACEMENT

Table 3.2: Patterned Catalysts

Catalyst	Suspended In	Results
Fe/Mo/alumina [3]	Methanol	Easy to pattern. Liftoff difficult. Slowly attacks PMMA mask. Appeared to promote to gate leaks through the SiO ₂ layer.
Fe/Mo/alumina [5]	IPA	Poor adhesion to substrate.
Fe/Mo/alumina [6]	DI water	Easy to pattern. Excellent adhesion. No gate leak problems.
FeCl ₃ [7]	DI water	Excellent adhesion to substrate. Not compatible with PMMA mask. Left substrate entirely covered in catalyst. May work well with PDMS stamp.
thermally evaporated Fe [8,9]	None	Very easy to pattern. Liftoff is clean. Difficult to control the thickness below 1 nm as required.

CHAPTER 3. GROWTH AND PLACEMENT

raphy. Catalyst is deposited in the following way:

1. Add the powder catalyst from Table 3.1 to 15 mL of DI water and stir for 12 hours
2. Sonicate the solution for 30 minutes
3. Cover the sample in catalyst solution for 30 minutes
4. Dry with N₂ gun
5. Liftoff by sonicating in acetone for 5 minutes, soaking in a clean acetone for 5 minutes, followed by an isopropanol rinse for 1 minute and a DI water rinse for 1 minute

Depositing the catalyst islands in a reproducible way proved to be the most difficult step in the fabrication of nanotube samples. It is suspected that baking the catalyst on a hot plate to dry the solution leads directly to gate leaks in the SiO₂ layers and later device failure. Thus, there is no baking step in the deposition of our catalyst islands.

3.2.2 Growth

The recipe for on-substrate growth of nanotubes used in this thesis is very similar to the growth recipe for powder catalyst discussed in Section 3.1.2. This recipe was developed over the course of several years from many points of reference [3,4,7,10–13]

CHAPTER 3. GROWTH AND PLACEMENT

and my own notes. The recipe is optimized for the 1 inch Lindberg tube furnace as seen in Figures 3.1 and 3.2. Most samples are placed in a smaller 1 cm diameter, 1 foot long quartz tube, then placed in the larger 1 inch diameter quartz tube. This was done to make the samples easier to load into the 1" tube, as well as to reduce turbulence in the gas flow across the sample [7].

The standard nanotube growth recipe used in this work is below:

1. Purge the tube by flowing 2000 sccm of Ar for 20 minutes
2. Heat the tube to 250 °C while flowing 300 sccm Ar and 150 sccm H₂
3. Wait for at least 1 hour
4. Heat the tube to 700 °C while flowing 300 sccm Ar and 150 sccm H₂
5. Wait for 10 minutes
6. Heat tube to 950 °C while flowing 300 sccm Ar and 150 sccm H₂
7. Wait for the temperature to stabilize
8. Flow 700 sccm CH₄ and 150 sccm H₂ for 10-15 minutes
9. Set temperature to 0 °C and let the furnace cool while flowing 300 sccm Ar and 150 sccm H₂

In almost every case this recipe has grown nanotubes successfully. Steps 2 and 3 are included to remove water vapor from the air that might have collected inside the

CHAPTER 3. GROWTH AND PLACEMENT

quartz tube on humid days [10]. Steps 4 and 5 are meant to remove iron oxide from the iron nanoparticles that make up the catalyst.

The most common point of failure has been related to the patterned molybdenum leads on the substrate. Molybdenum oxidizes rapidly at high temperatures. Therefore, any oxygen contamination in the tube during the growth process will form a MoO layer that is then quickly removed by reacting with the high temperature H₂ flow. This process repeats and can lead to the Mo leads being entirely etched away. Additionally, it has been found that opening the furnace too soon during cooling can lead to the Mo leads peeling off of the substrate. This appears to be caused by some super-heating due to IR radiation reflecting off of the surfaces of the sample and quartz tube. It is a strange phenomenon that is avoided by allowing the furnace to cool to less than 300 °C before opening the lid. These problems could also be solved by using a different high temperature metal such as a W/Pt bilayer, common in many other nanotube projects. Molybdenum was chosen for this work because it is easy to sputter and much more affordable.

3.2.3 Conclusion

Growing nanotubes from catalyst islands near predefined leads and markers offers a huge improvement over the method of random dispersion. Nanotubes produced with this method are longer, cleaner, and easier to locate. These improvements, along with the ability to produce many more samples in much less time, made this method the

CHAPTER 3. GROWTH AND PLACEMENT

obvious choice for device fabrication.

3.3 Imaging Nanotubes

Nanotubes on a SiO₂ surface can be located in a number of ways. This section will review a number of different methods, focusing on improvements made in the course of this thesis work.

3.3.1 Atomic Force Microscopy

With nanotubes that have been drop cast onto the surface, the standard method is to locate the tubes relative to the predefined markers using a tapping mode atomic force microscope (AFM). An example of an image created this way is seen in Figure 3.5.

This method is very reliable, but extremely time consuming. In order to resolve nanotubes, as well as the predefined markers in the image, AFM scan sizes must be limited to 25 μm^2 . Each of these scans takes 30 minutes and many scans are needed to fully image one patterned substrate. Looking closely at Figure 3.5, there are 12 scans covering less than half the substrate. Due to vibrational noise and piezo limits, some images are slightly warped. Stitching the images together is time consuming and inaccurate.

CHAPTER 3. GROWTH AND PLACEMENT

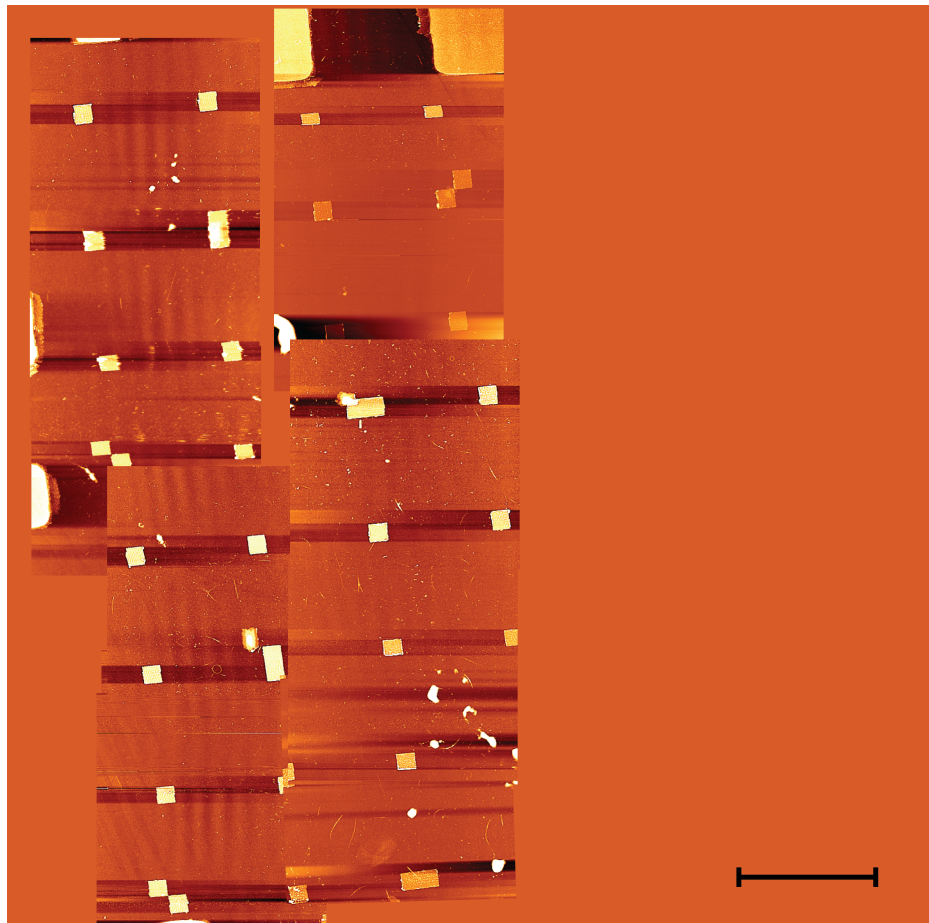


Figure 3.5: A composite image made from several AFM height measurements of a sample with nanotubes dispersed over a substrate with $1.5\text{ }\mu\text{m}$ gold markers. The scale bar is $10\text{ }\mu\text{m}$.

CHAPTER 3. GROWTH AND PLACEMENT

3.3.2 Electric Force Microscopy

The Digital Instruments Nanoscope 3 used in our lab is also capable of making electric force microscope (EFM) measurements. An EFM image is made by first measuring the height across the sample in standard tapping mode, then using that height data to run a second 'interleave' scan at a fixed height with a bias voltage applied between the tip and sample. By holding the tip at a fixed height, van der Waals interactions between the tip and sample are constant and the only force measured is the electrostatic force from the applied bias voltage. Contrast in the resulting images is related to the different conductivities of the objects on the sample [14]. Thus, conducting (and semiconducting) nanotubes have a high contrast against the insulating SiO₂ substrate. An example of this type of image is shown in Figure 3.6

An entire patterned substrate can be scanned using this method in about 1 hour. The scan size can be increased up to 75 μm² due to the false contrast provided by the large electrostatic forces between the nanotubes and the tip. Rather than appearing as 1 nm in diameter, the tubes appear in the EFM image to be about 100 times their real diameter. This was a notable improvement over locating nanotubes using AFM height scans alone. Comparing Figure 3.5 and Figure 3.6, it is clear the EFM image is far more useful in locating nanotubes.

CHAPTER 3. GROWTH AND PLACEMENT

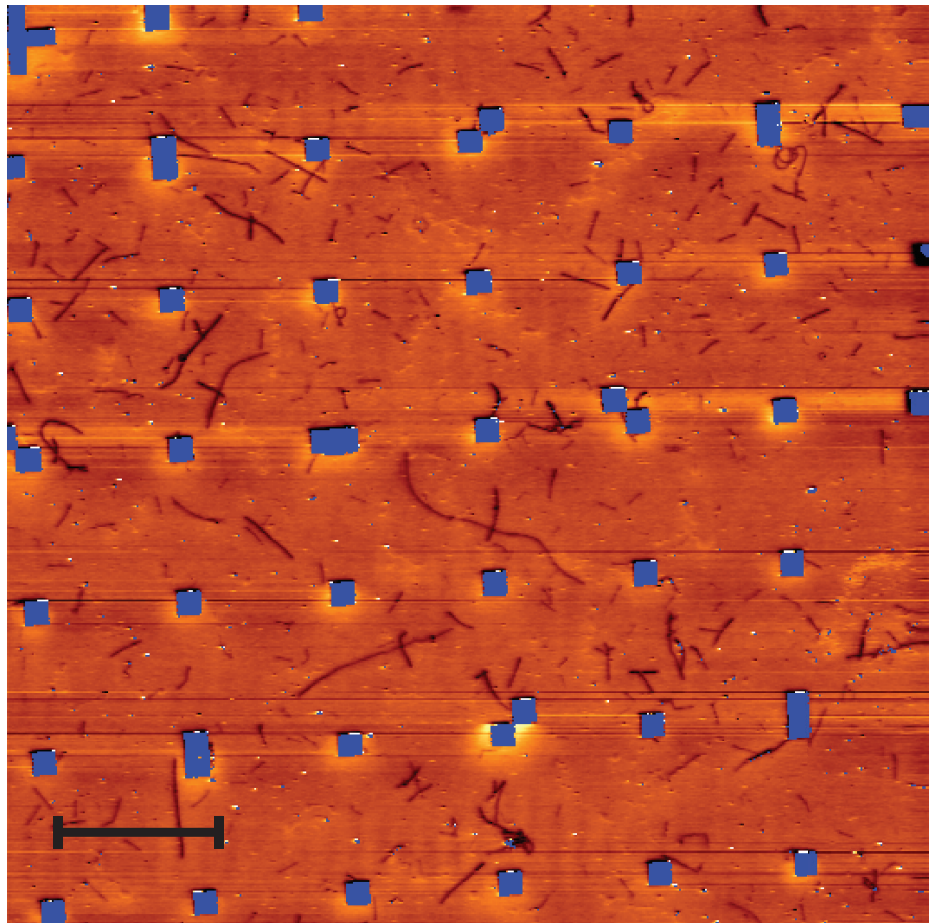


Figure 3.6: An EFM image of nanotubes dispersed over a substrate with $1.5\text{ }\mu\text{m}$ gold markers. The markers have been automatically located using the height data and highlighted in blue on the EFM image. The scale bar is $10\text{ }\mu\text{m}$.

CHAPTER 3. GROWTH AND PLACEMENT

3.3.3 EFM Through PMMA

All of the same techniques from Section 3.3 can be applied to imaging nanotubes grown from patterned catalyst islands. However, because the substrates are not covered in closely spaced markers, it was found that tapping mode AFM height scans were not useful. Scans could only cover a small part of the sample and the resulting images were difficult to orient.

Using electric force microscopy (EFM) made it possible to scan the entire region of interest on the sample in one measurement. An example of this type of scan is shown in Figure 3.7a. As can be seen in that figure, it was difficult for the AFM tip to avoid crashing into the catalyst islands during the EFM sweep. The catalyst islands are several hundred nanometers in height while the other features on the substrate are less than 10 nm. Such height differences make large area scans difficult in tapping mode. This problem can be avoided by coating the sample in PMMA before scanning with the EFM, as seen in Figure 3.7b. The PMMA coating smooths the height differences between the substrate and catalyst islands, without compromising the contrast between the insulating substrate and conducting nanotubes. The idea was adopted from a 2007 paper in which the authors attempted to locate nanotubes suspended in a PMMA layer in three dimensions [15].

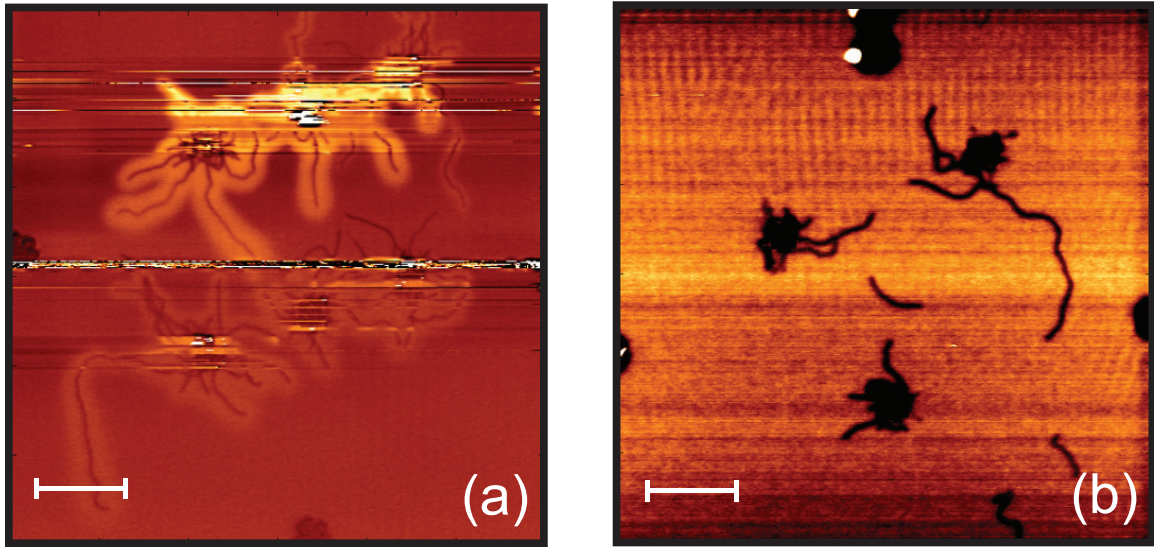


Figure 3.7: (a) Frequency data collected from an EFM scan of a catalyst island sample after nanotube growth. (b) Frequency data collected from an EFM scan of a similar sample. Prior to the scan this sample was coated with a 250 nm PMMA layer. Both scale bars are 10 μm .

3.3.4 Scanning Electron Microscopy

In 2002, a paper [16] was published illustrating that a scanning electron microscope (SEM), operating at a low accelerating potential could provide a similar type of false contrast image as produced by the EFM. The insulating substrate tends to collect charge from the electron beam, while the conducting nanotubes do not. This produces an image in which the nanotubes appear as bright lines about 100 times their actual diameter. An example of this is seen in Figure 3.8.

Typically, an EFM scan of a sample will take 45 minutes. A SEM image of the same sample takes less than 2 minutes. However, the SEM can introduce some carbon contamination from the high energy electrons passing through small amounts of oil mist back-streaming into the vacuum chamber from the mechanical roughing pump.

CHAPTER 3. GROWTH AND PLACEMENT

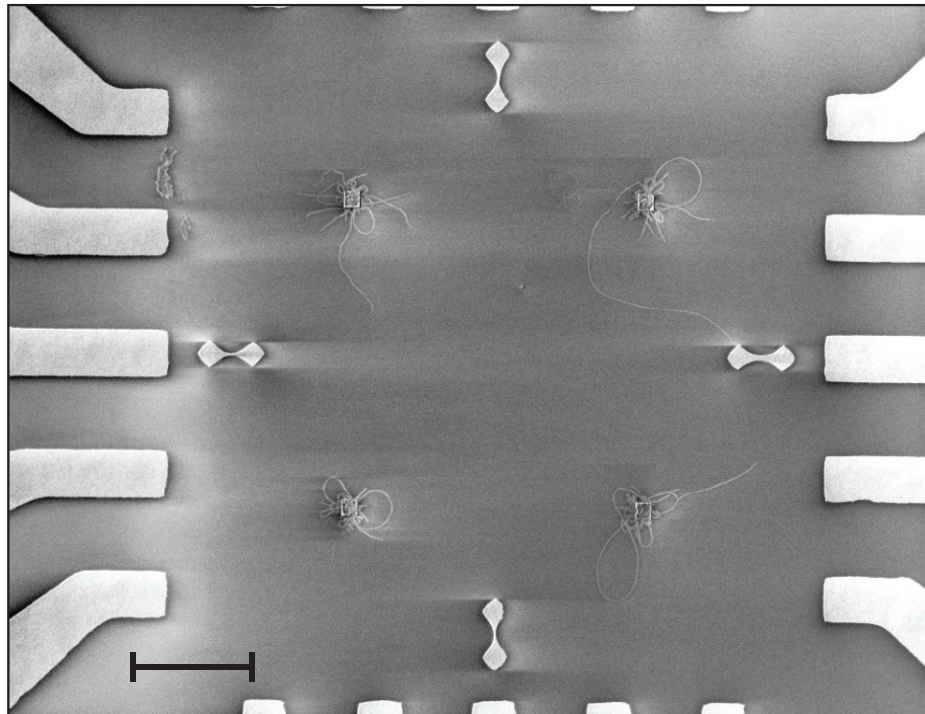


Figure 3.8: A scanning electron micrograph of a catalyst island sample after nanotube growth. The scale bar is 10 μm .

CHAPTER 3. GROWTH AND PLACEMENT

Due to the large number of samples that were produced to obtain the data in this thesis, it was decided that contamination from the SEM was an acceptable risk, given the immense time savings.

3.4 Image Filtering

Once it became clear that the scanning electron microscope was by far the most efficient and reliable way to locate carbon nanotubes on a substrate, it also became important to optimize those images to reveal the most information possible. The resolution and contrast in the SEM images produced in our lab are limited by the use of a thermionic LaB₆ filament. Unlike field emission scanning electron microscopes, which are more common in nanofabrication, the thermionic scanning electron microscope has a large initial crossover size, requiring more electromagnetic lens focusing to produce a sufficiently small beam size for imaging. This problem is exasperated when using low accelerating potentials (500-3000 V), which are crucial to achieving good contrast of carbon nanotubes on a silicon substrate.

3.4.1 Histogram Equalization

This method was based on two corrections. First, a plane fit to correct for the position of the secondary electron detector. Second, finding the histogram then transforming it such that there are equal numbers of pixels at each brightness level. An

CHAPTER 3. GROWTH AND PLACEMENT

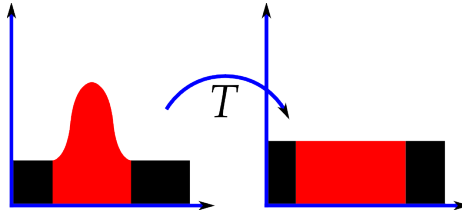


Figure 3.9: An illustration of the histogram equalization process.

illustration of this can be seen in Figure 3.9

Figure 3.10 shows the process of filtering an SEM image using histogram equalization. At the top of figure is the original image after a plane fit (to correct changes in brightness across the substrate). To the right of the image, the histogram of brightness values and the cumulative distribution function are plotted. The center image is after the histogram equalization. Contrast is now dramatically increased in the image, the histogram is nearly flat, and the cumulative distribution function is linear. Finally, the image is gaussian filtered using a 3×3 kernel to reduce the high frequency noise, which has been exaggerated by the histogram equalization. The final histogram is not flat quite flat and the cumulative distribution function is not quite linear. However, the contrast in the image has been enhanced significantly

While this filter does success in increasing contrast in the image, which was the main problem associated with our SEM, it also increases the background noise to often unacceptable levels. Histogram equalization does not use any specific information about the carbon nanotubes and substrates being imaged. A better filter should be possible by taking advantage of the fact that the features of interest can be well

CHAPTER 3. GROWTH AND PLACEMENT

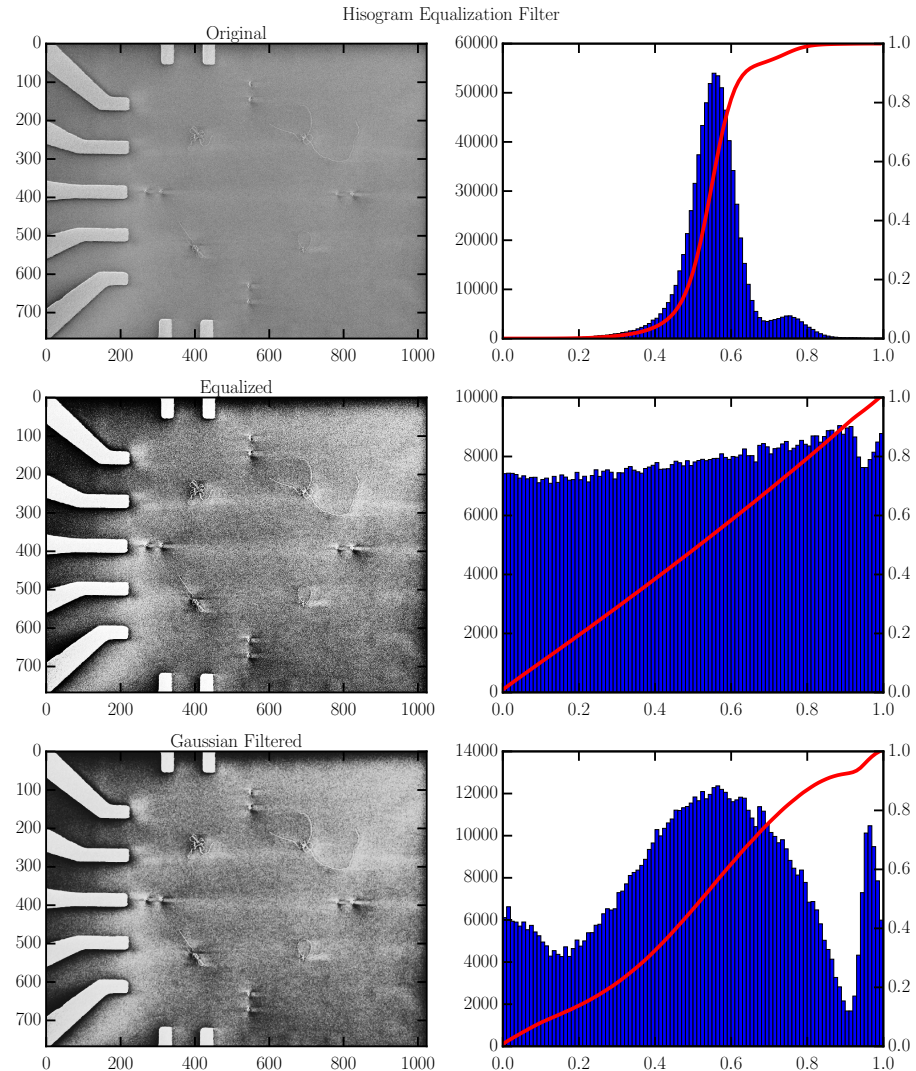


Figure 3.10: Top image is the original SEM image after a plane fit. Middle image shows the SEM image after histogram equalization. Bottom image shows the final result after gaussian smoothing. Plots on the right show the histogram of brightness values and cumulative distribution function at each step.

CHAPTER 3. GROWTH AND PLACEMENT

characterized in a sample set of images.

3.4.2 Matched Filter Bank

Matched filter banks are a well known technique that have been used very successfully to filter retinal images in medicine [17]. This technique has previously been adapted to high resolution SEM images of carbon nanotube bundles [18]. The following section describes the implementation of this method to filter images of single walled carbon nanotubes grown on insulating substrates.

3.4.2.1 Nanotube Profile Model

To begin building the matched filter bank, the profile shape of a single nanotube from the SEM image must be determined. To find this shape, a random set of 25 SEM images was selected (similar to those in Figure 3.8). From each of these images, images of two nanotubes were cropped. Those nanobues can be seen in Figure 3.11a. Each of these images was then rotated such that the longest straight portion (that could be identified by eye) was oriented vertically. The profile of the nanotube was averaged over that long straight section. These results are plotted in Figure 3.11b.

Based on the shape of these profiles a truncated *sinc* function, Equation 3.1, was chosen to fit the nanotube profile.

CHAPTER 3. GROWTH AND PLACEMENT

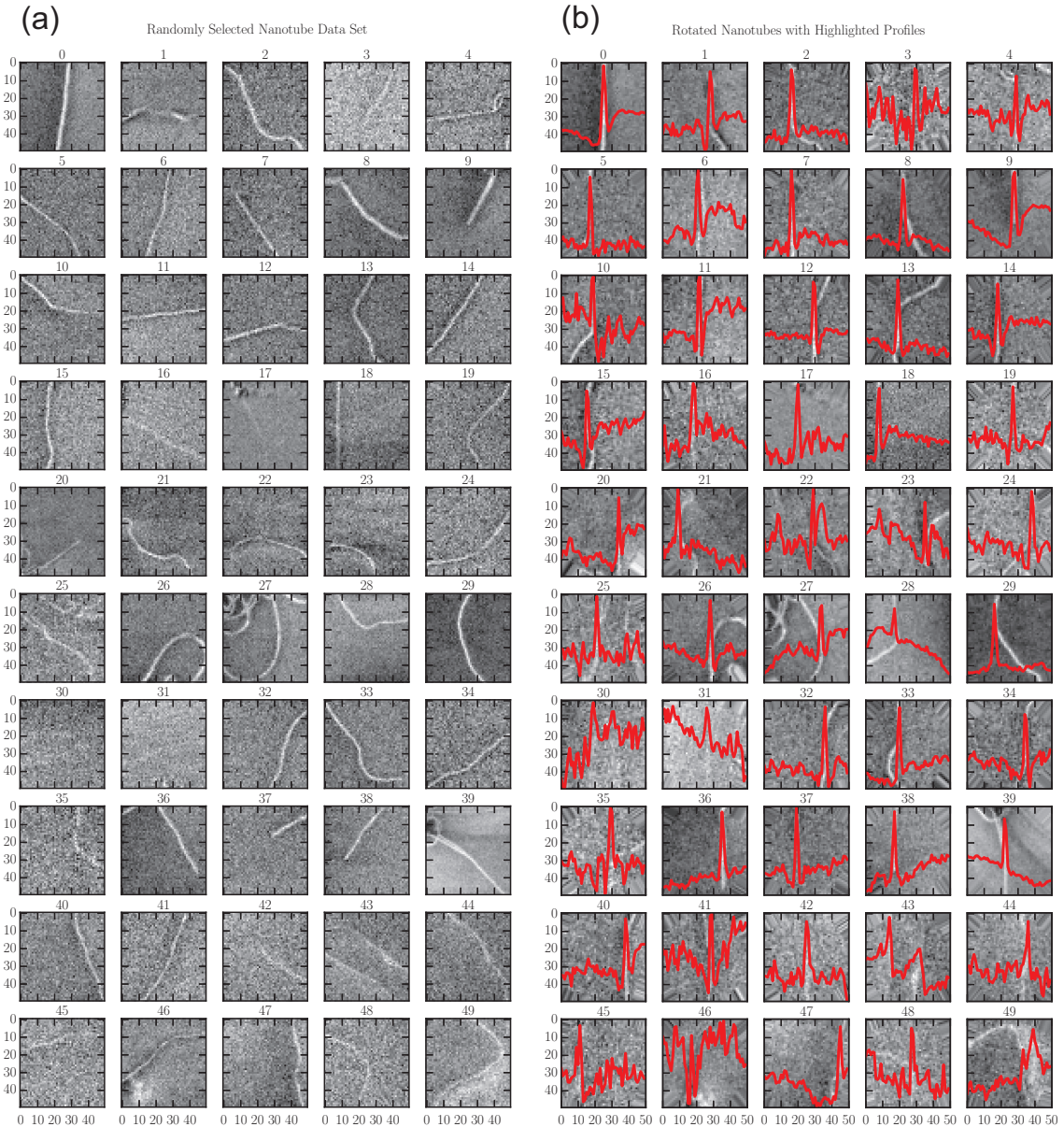


Figure 3.11: a) The original data set of SEM nanotube images used to create and optimize the matched filter bank. b) The same data set rotated and overlaid with extracted nanotube profiles.

$$f(x) = \begin{cases} \frac{A \sin kx}{kx} & |x| < \frac{2\pi}{k} \\ 0 & |x| > \frac{2\pi}{k} \end{cases} \quad (3.1)$$

This function was chosen because it captures the bright nanotube peak and dark regions beside the nanotube while still only requiring one fit parameter. To determine the fit parameters the linear background was subtracted from each profile in Figure 3.11b and the profiles were fit using 3.1. The results of this fitting can be seen in Figures 3.12a and b.

3.4.2.2 Filter Kernel

The filter kernel is built starting with the median k value found from the profile fits. To extract each profile, horizontal cuts of the nanotube image were averaged over a straight segment of the nanotube that was identified and labelled by hand. The distribution of these straight segment lengths can be seen in Figure 3.12c. Again, to proceed with building the filter we use the median value of L from that distribution. The kernel is built in an $N \times N$ matrix with $(x, y) = (0, 0)$ at the center of the matrix. The full kernel, $K(x, y)$ is defined by Equation 3.2.

$$K(x, y) = \begin{cases} \frac{A \sin kx}{kx} & |x| < \frac{2\pi}{k}, |y| < \frac{L}{2} \\ 0 & |x| > \frac{2\pi}{k}, |y| > \frac{L}{2} \end{cases} \quad (3.2)$$

Once the kernel is defined on the $N \times N$ matrix, the kernel is normalized such that

CHAPTER 3. GROWTH AND PLACEMENT

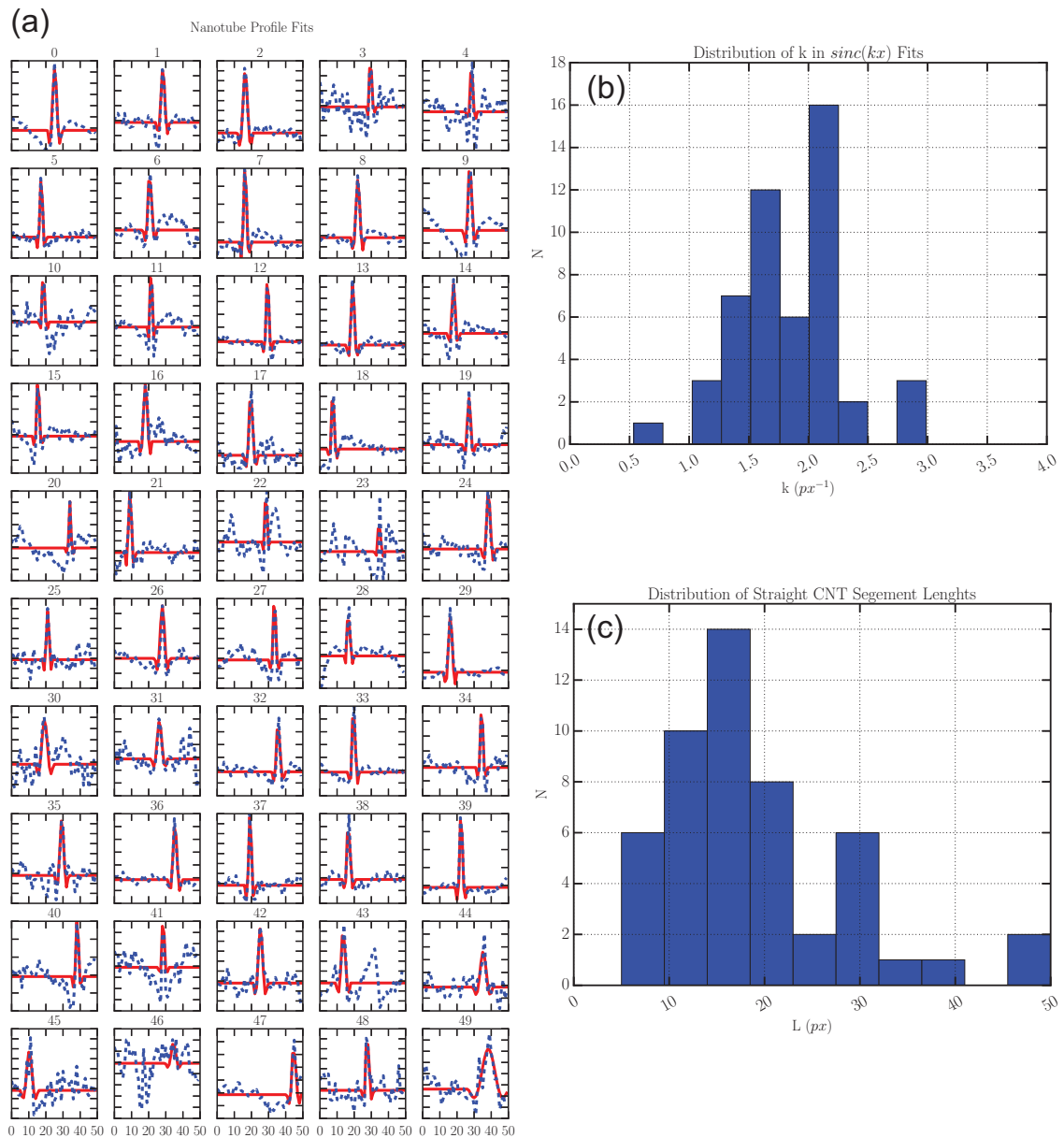


Figure 3.12: a) Extracted nanotube profiles with linear background removed (blue). Fits to 3.1 (red). b) Distribution of k values extracted from profile fits. c) Distribution of straight nanotube section lengths.

CHAPTER 3. GROWTH AND PLACEMENT

the sum over all of the matrix elements is equal to zero. By convolving this kernel with the SEM image, portions of the image with a shape matching the fit profile and a length L will be highlighted in the output. This results in significant background subtraction and accurate nanotube enhancement.

3.4.2.3 Filter Bank

To build the full filter bank, the kernel, built using Equation 3.2, is rotated by a set of angles between 0 and π . Each of these filters is then convolved with the image separately. By doing this, it is possible to identify nanotube sections lying along any direction on the substrate. A binary result is created using thresholding on the convolved image. The filter bank and resulting binary images can be seen in Figures 3.13c and d.

After each kernel has been separately convolved with the original image, and the threshold applied, those binary images are added together to produce the final filtered image. Figures 3.13a and b show the original and filtered nanotube images.

In building this filter many parameters had to be optimized simultaneously and compared by eye. Due to the large parameter space, the matched filters were optimized by iteratively varying a single parameter and choosing the best result. This process is illustrated in Figure 3.14.

The results of this optimization are seen in Table 3.3. The optimized values for k and L were very close to those obtained from the original analysis of extracted

CHAPTER 3. GROWTH AND PLACEMENT

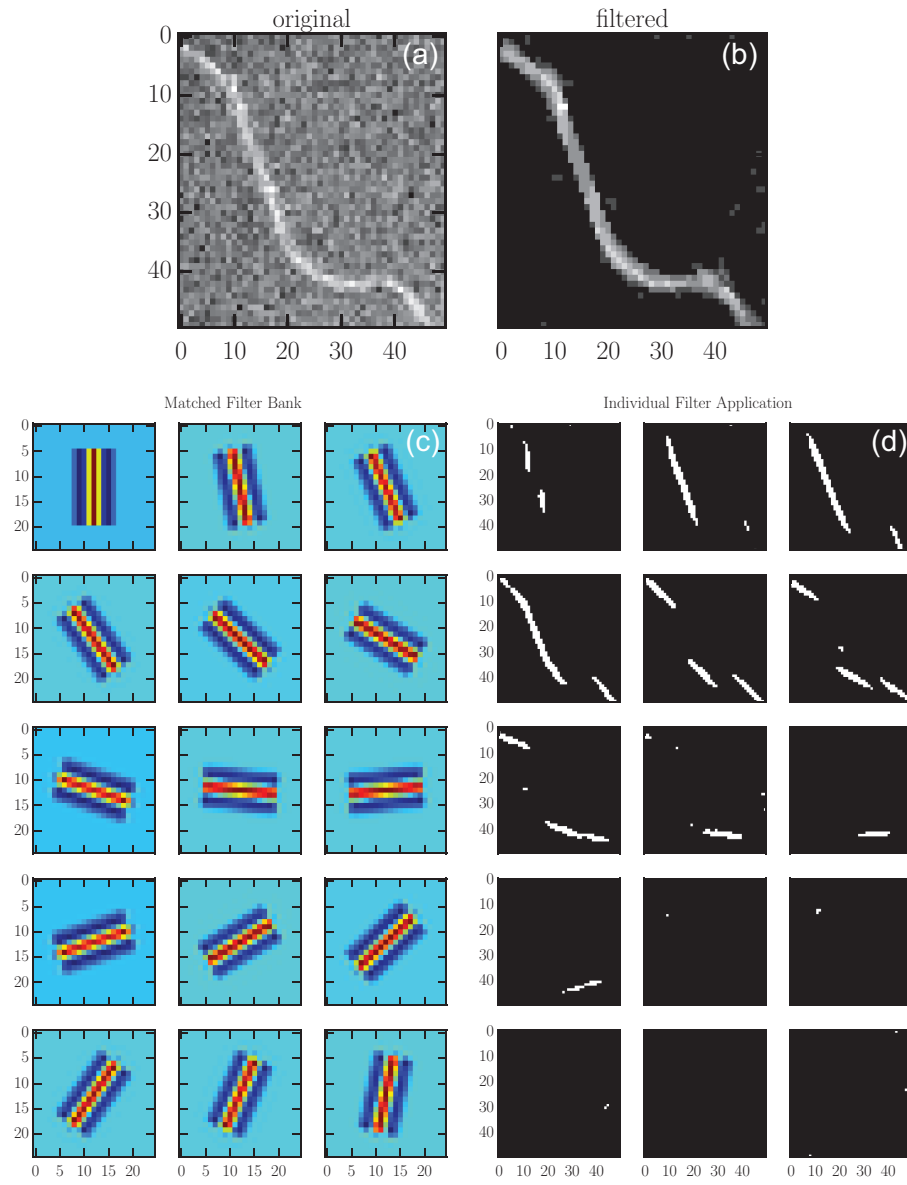


Figure 3.13: a) Original image. b) Final filtered image, which is the sum of the binary images in (d). c) The rotated kernels that form the full matched filter bank. d) Each rotated kernel applied to an image in (a).

CHAPTER 3. GROWTH AND PLACEMENT

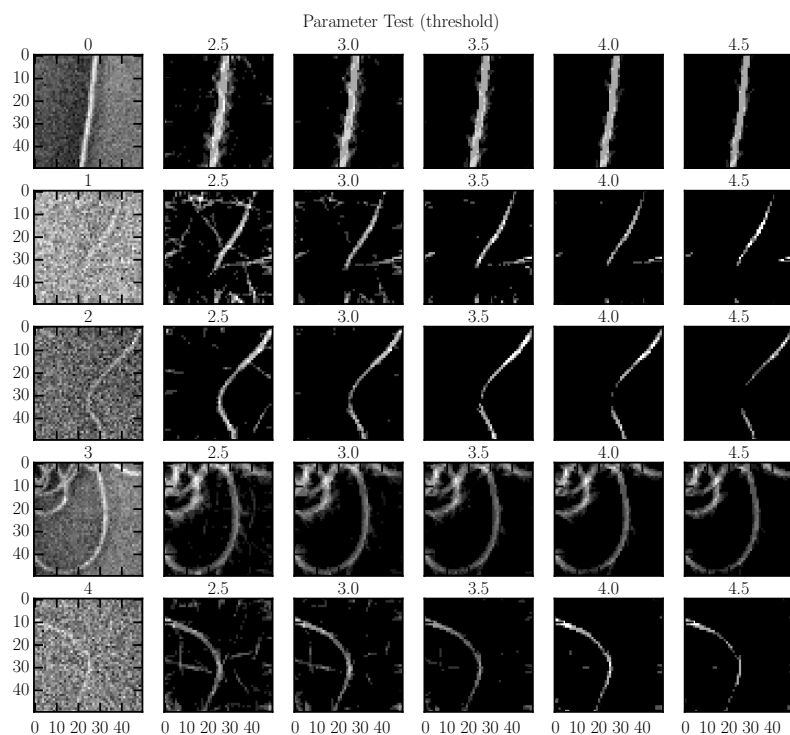


Figure 3.14: Optimization of the matched filter bank threshold value.

CHAPTER 3. GROWTH AND PLACEMENT

Table 3.3: Matched Filter Bank Parameters

Parameter	Description	Optimized Value
k	inverse length scale for <i>sinc</i> fit	$1.75px^{-1}$
A	height of <i>sinc</i> function in $K(x, y)$	10
L	length of straight nanotube sections to search for	$16px$
N	size of the kernel matrix	25
R	number of kernels in the filter	15
threshold	cutoff value for thresholding images convolved with filter kernels	3.6

nanotube profiles. Note that A and *threshold* are not independent values and A remained fixed for this optimization procedure.

It is also important to note that the length scale for these parameters is in pixels (px). The randomly selected SEM images that were used for this analysis were not all taken at the same magnification level. However, the average magnification was $850\times$ giving a pixel size of $\sim 140\text{ nm}$

Finally, the filter was tested with the original set of full device SEM images. A selection of the results can be seen in Figure 3.15. It is clear from this set of images that the filter has the desired result. Nanotubes are much more clearly visible and the background is almost completely removed. Because the filter is very similar in

CHAPTER 3. GROWTH AND PLACEMENT

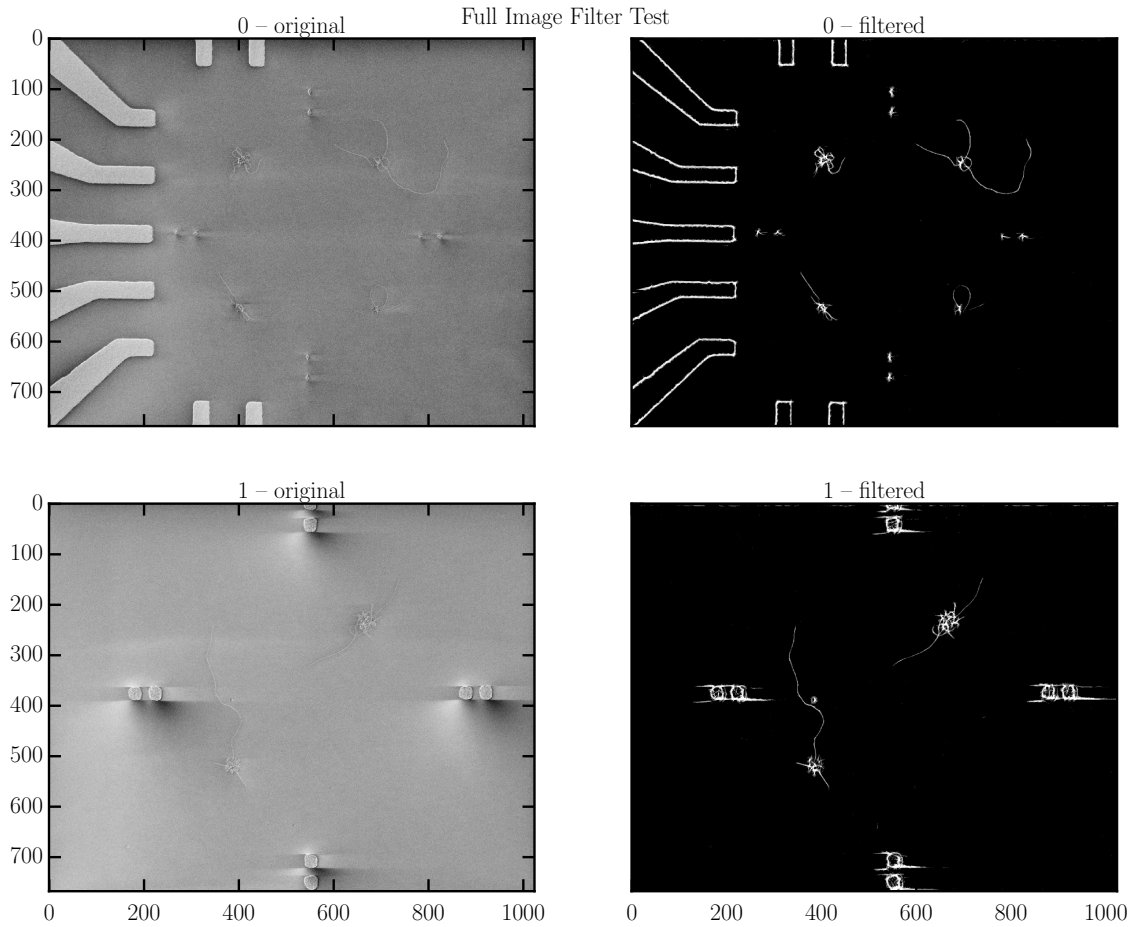


Figure 3.15: Optimization of the matched filter bank threshold value.

it's construction to common edge detection algorithms, it also leaves features at the edges of the optical lithography leads and markers defined on the substrate before nanotube growth. This actually works well since those features are used to align the SEM images for additional electron beam lithography steps.

Chapter 4

Metallic Contacts to Carbon Nanotubes

Chapter will contain: an explanation of the nature of metal-nanotube interfaces, statistics on metals tested, thin film deposition methods, and lithography methods. opinions will be backed up with a lot of histograms, contact resistance data, and device images. It's not the most exciting chapter, but it is what I spent a great deal of time thinking about over the past two years.

Chapter 5

Quantum Dots with Ferromagnetic Leads

Four samples to discuss here that looked very good. SCF72, SCF75, SCF96, SCF98. The first two show some evidence of splitting at a persistent field, possibly some MR behavior. The second two show some interesting co-tunneling peaks that are suppressed at non-zero field.

Chapter 6

Spin Transport in Tunable Ferromagnet/Superconductor Junction

Two samples to discuss. MT7 and scfmh8 (possibly scfmh2,5 as well). Low resolution Bias/Field sweeps of MT7. Interesting switching behavior in scfmh8 at low field.

Appendix A

Fabrication Details

This appendix describes, in detail, each of the steps taken to create the carbon nanotube (nanotube) devices measured for this thesis. Some of the information is specific to the Markovic lab and Johns Hopkins University, but an effort has been made to make the discussion useful to anyone producing nanotube devices.

The devices measured in this thesis were all produced with the following recipe:

1. Use the mask aligner (A.1.2.2) to pattern large sputtered molybdenum (A.4.3)
leads on a silicon substrate
2. Pattern small catalyst islands (3.2) using electron beam lithography (A.3)
3. Grow nanotubes directly on substrate using chemical vapor deposition (3.2.2)
4. Locate nanotubes using a scanning electron microscope (3.3.4)
5. Design devices using vector graphics software (A.2)

APPENDIX A. FABRICATION DETAILS

6. Pattern devices using electron beam lithography (A.3) and thin film deposition (A.4)
7. Test device connectivity in the DC probe station (A.5.1)
8. Wire bond connected devices in a chip carrier for further testing (A.5.2)

For details on each of the steps see the sections referenced. The rest of this appendix discusses additional methods and contains some useful observations made over several years spent producing nanotube devices.

A.1 Wafer Preparation

Each nanotube device began with a highly doped silicon substrate capped with an insulating layer. The wafers used were chosen for their low temperature electrical properties and ease of use.

A.1.1 Selection and Cleaning

All of the devices discussed in this thesis were built on highly n-doped silicon wafers with SiO_2 capping layers. The wafers were purchased from Silicon Quest International. As ordered the wafers are 3 inches in diameter with a $<100>$ silicon face. This crystal alignment allowed the wafers to be easily cleaved along the crystal axes using only a diamond scribe. The wafers are heavily n-doped with phosphorus

APPENDIX A. FABRICATION DETAILS

giving them a resistivity of $10\text{-}20\,\Omega\text{cm}$ down to the milliKelvin range. The oxide layers were 300\AA of thermally grown SiO_2 and remained insulating at all measured temperatures.

Typically, wafers were cleaned by sonicating in acetone for 5 minutes, followed by an isopropanol rinse for 1 minute, and baking on a hot plate at about $180\text{ }^\circ\text{C}$ for 1 minute. This procedure was usually enough to ready the surface for lithography. In cases where cleanliness had to be improved, piranha etch was used to clean the wafers.

Piranha etch is a mixture of 3:1 30% sulfuric acid to 30% hydrogen peroxide. It is important to be extremely careful with this wet etch as the solution is strongly exothermic. The wafers should be placed in the sulfuric acid, then the hydrogen peroxide is added slowly while stirring continuously. The solution will reach nearly $200\text{ }^\circ\text{C}$ within the first few minutes. After about 20 minutes, the solution should cool enough for the wafers to be removed. Surfaces cleaned in this way are free of organic and most metallic contaminates.

A.1.2 Optical Lithography

The first step in building the devices discussed in this thesis was to pattern the substrate using optical lithography. In this process the wafer is first coated in a UV sensitive polymer resist. The wafer is then partially exposed to UV light and developed, leaving a patterned polymer mask through which thin films can be deposited.

APPENDIX A. FABRICATION DETAILS

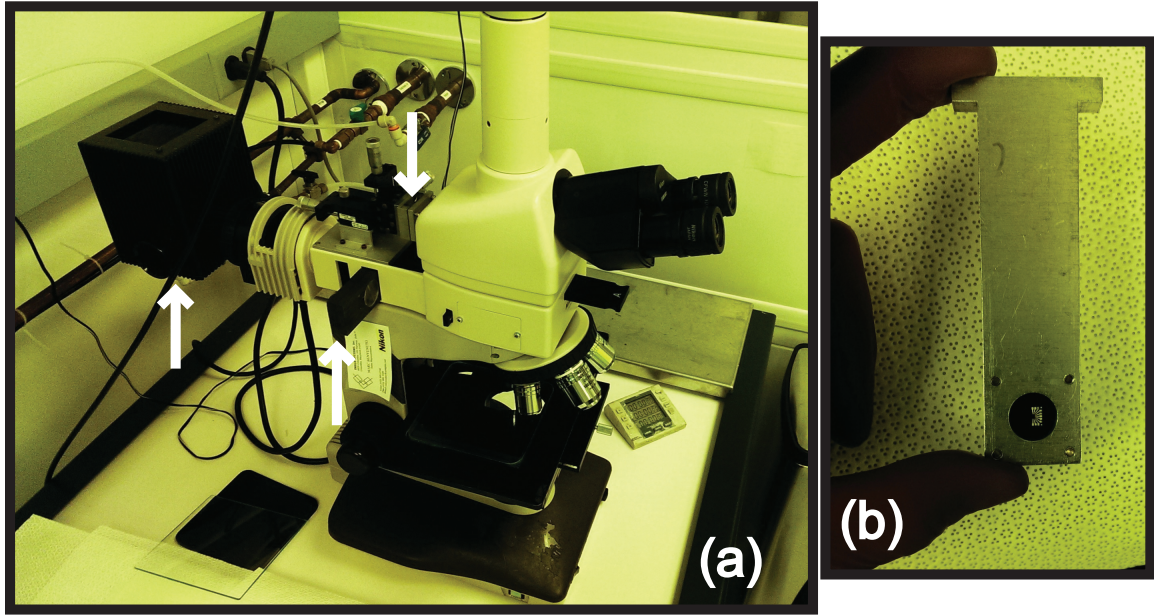


Figure A.1: Custom projection lithography setup in the JHU physics department cleanroom. (a) The arrows from left to right show the UV lamp, sliding UV filter, and mask holder. (b) A projection lithography mask and holder. The arrow shows the mask itself.

The resists used can be either positive or negative tone. For this work, MicroChem S1813 was used as a positive tone resist and Futurex NR9 was the negative tone resist. Exposure, baking, and development times were chosen according to the manufacturer's instructions.

A.1.2.1 Projection Lithography

Many of the devices produced in the Markovic lab have been patterned using the custom built projection lithography setup seen in Figure A.1. The setup was built around a Nikon optical microscope. The microscope has been fitted with a UV lamp, movable UV filtering, and a custom mask holder.

APPENDIX A. FABRICATION DETAILS

The masks were made using either a standard ink-jet printer or by a local printing company for higher resolution. The sample is placed under the desired objective, which determines the size of the pattern projected onto the sample. The mask is then inserted into the holder and then focused and positioned using the micrometer drives. Exposure times are controlled by removing the UV filter from the light path.

This setup is useful for quickly producing a few samples at a time. Specifically, it is used for producing graphene and nanowire devices, which require careful positioning of the pattern over the nanostructure of interest. The resolution limit of this technique is about $2\text{ }\mu\text{m}$.

A.1.2.2 Mask Aligner

For production of many, identical devices, projection lithography as described in Section A.1.2.1 becomes extremely tedious. This problem was solved by use of a mask aligner.

First, a chromium on glass mask is made with the desired pattern in the actual size, as seen in Figure A.2. The mask is then loaded into the aligner and a substrate, coated with polymer resist, is mounted under it. Finally, the mask and substrate are pressed together and exposed to a UV light source. The resolution of the OAI mask aligner is about $1\text{ }\mu\text{m}$.

APPENDIX A. FABRICATION DETAILS

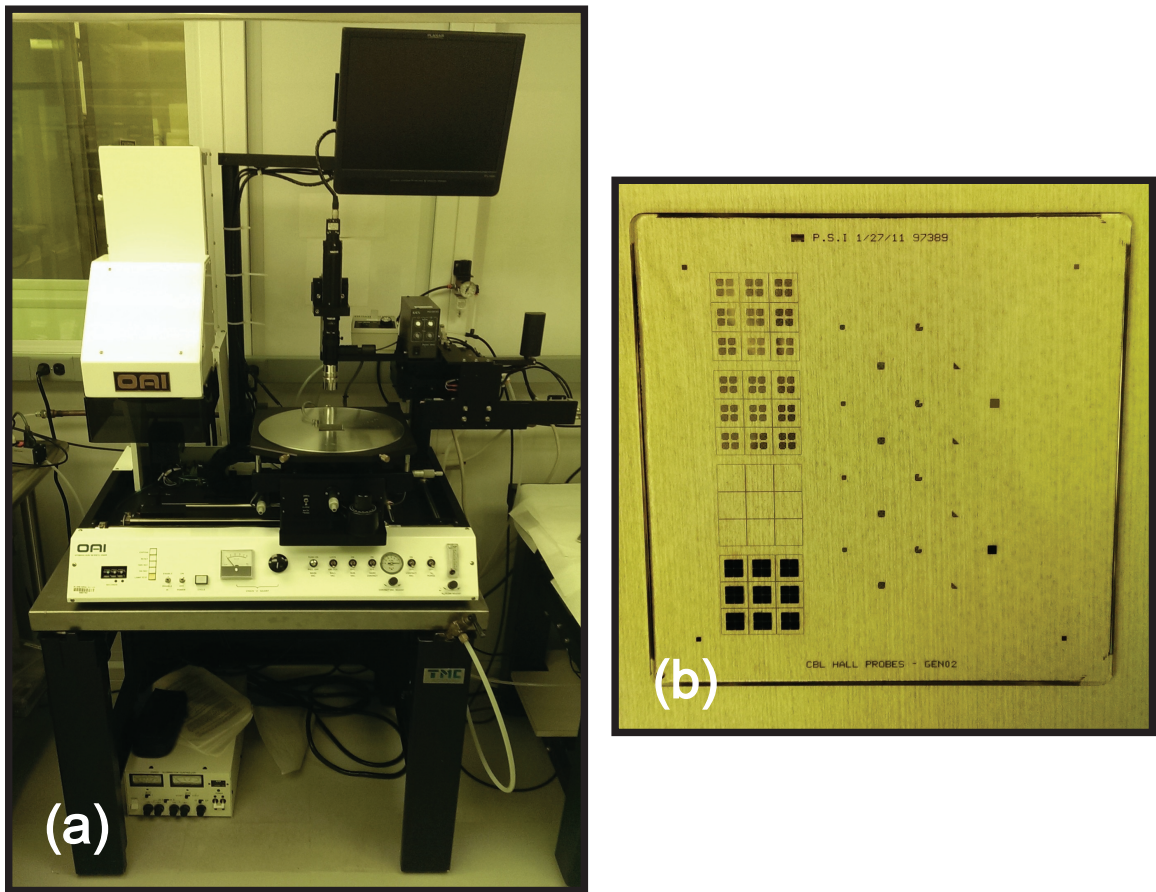


Figure A.2: OAI mask aligner in the JHU physics department cleanroom. (a) The mask aligner. (b) A typical 3" chromium on glass mask.

APPENDIX A. FABRICATION DETAILS

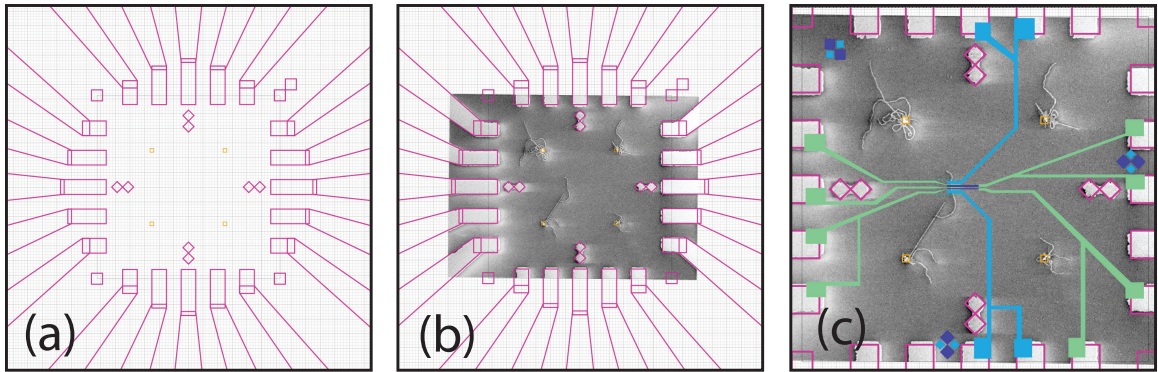


Figure A.3: Adobe Illustrator designs used for optical and electron beam lithography masks. (a) The pink outlines show the large molybdenum leads patterned with the mask aligner. Inside that pattern are the four $3\text{ }\mu\text{m}$ catalyst islands patterned with electron beam lithography. (b) An SEM micrograph of a sample after CVD growth fitted into the pattern. (c) A complete circuit design. In this case, the layers are normal metal (green), ferromagnet (purple), and superconductor (blue).

A.2 Device Design

Once the substrates are prepared, devices are designed one at a time using Adobe Illustrator. Any computer aided drafting (CAD) or vector graphics program would work just as well. The procedure is outlined in Figure A.3. Designing the devices is a simple process of connecting the nanotubes with the mask aligner leads, although some thought must be given to the size of the leads drawn. If the leads are too large, the write time for the electron beam lithography steps will be too long. Additionally, one must be careful not to let any stray nanotubes short the device leads.

APPENDIX A. FABRICATION DETAILS



Figure A.4: Zeiss EVO50 SEM with Raith control computer and external beam blanker.

A.3 Electron Beam Lithography

Electron beam lithography is the process of creating masks by patterning a polymer resist by exposure to a focused beam of electrons. In the Johns Hopkins physics department the electron beam lithography setup is based around a Zeiss EVO50 scanning electron microscope. The microscope is controlled by Zeiss SmartSEM software. Attached to the microscope control computer by a serial port is a second computer running Elphy Quantum, electron beam lithography software from Raith. The Raith software can take control of the beam to write patterns based on GDSII drawings. The SEM setup is shown in Figure A.4.

The electron beam sensitive resist used in all of this work was polymethyl

APPENDIX A. FABRICATION DETAILS

Table A.1: Standard PMMA/MIBK recipe

EHT Voltage	30 keV
Beam Current	40 pA
Step Size	10 nm
Dose	300 $\mu\text{C cm}^{-2}$
Developer	1:3 MIBK:IPA
Development time	60s
Post-development	rinse 30s in IPA

methacrylate (PMMA) from MicroChem. PMMA is a polymer that, after baking on a hot plate, forms copolymer bonds that can be broken by exposure to a beam of electrons. Once these bonds are broken, the unbonded polymer can be washed away by a developer, leaving trenches in the PMMA wherever it was exposed to the electron beam. The patterned mask can later be removed by soaking in acetone.

A.3.1 Standard Recipe

This recipe, using room temperature methyl isobutyl ketone (MIBK) as a PMMA developer, is the simplest recipe to start with for almost any project requiring electron beam lithography. The relevant parameters are shown in Table A.1.

APPENDIX A. FABRICATION DETAILS

Table A.2: Cold developer recipe

EHT Voltage	30 keV
Beam Current	40 pA
Step Size	10 nm
Dose	$1400 \mu\text{C cm}^{-2}$
Developer	7:3 IPA:water at 0°C
Development time	90s
Post-development	rinse 30s in water

A.3.2 Cold Development

It was discovered in 2004, that by lowering the development temperature and increasing the dose, the resolution of PMMA could be improved significantly [19]. This has been shown using MIBK:IPA as a developer as well as various mixtures of IPA and water [20–23]. The best results obtained in our lab were using IPA and water. The recipe is shown in Table A.2. The improved contrast can be attributed to the higher dose. By increasing the dose and decreasing the efficacy of the developer, the negative effects of backscattered electrons passing through the PMMA are diminished.

APPENDIX A. FABRICATION DETAILS

A.4 Thin Film Deposition

In this work, thin film deposition is used (along with polymer masks patterned with optical or electron beam lithography) to create circuits around carbon nanotubes. There are three main methods used; each method will be discussed along with a few materials typically deposited in that way.

A.4.1 Thermal Evaporation

Thermal evaporation is the simplest method of thin film deposition discussed here. The material to be evaporated is placed in a boat, typically made of tungsten, alumina, or both. Substrates for the film to be deposited on are located above the evaporation boat. Both the boat and the samples are placed in a high vacuum chamber. Once the chamber has reached around 1×10^{-7} Torr, current through the evaporation boat is increased until the material melts or begins to sublime. The deposited thickness and deposition rate are monitored using a quartz crystal monitor. Once the desired rate is reached, a shutter is opened to expose the sample to the evaporated material.

This type of evaporation is best used with materials that have a relatively low melting point ($\lesssim 1200^\circ\text{C}$). Two evaporators were used in this work, a 1970s Denton evaporator fitted with a newer Hewlett Packard power supply, and an early 2000s Torr thermal evaporator. The Torr chamber is kept free from magnetic materials in

APPENDIX A. FABRICATION DETAILS

Table A.3: Thermal evaporation materials

Au	alumina coated W crucible
Ti	long, narrow W boat
Cr	chrome plated W rod
Al	dimpled W boat
Co	alumina coated W crucible (does not last long)

hopes of limiting contamination of superconducting films. Some common materials and the boats we have found most useful are listed in Table A.3.

A.4.2 Electron Beam Evaporation

Electron beam evaporation uses a high energy (7.5 keV) beam of electrons to melt the source material. The electron gun sits under a crucible full of the source material. The electron beam generated is bent and rastered across the center of the crucible using a strong magnetic field. Substrates are placed above the crucible and as the material melts and evaporates it is deposited on the substrate.

This method of evaporation has two benefits over thermal evaporation. First, it can be used for materials with a higher melting point. In the case of the Sharon Vacuum electron beam evaporator used in this work, materials with melting points up to $\sim 1800^{\circ}\text{C}$ were successfully evaporated. Second, the evaporated films are typically

APPENDIX A. FABRICATION DETAILS

a little cleaner because the crucible, unlike thermal evaporation boats, does not have to be heated in order for the source material to melt.

Due to limited access to the evaporator, not many of the films discussed in this work were deposited with electron beam evaporation. However, we have successfully deposited Nb, Co, Ti, and Al films all from graphite crucibles. Graphite was chosen here because of its affordability. There are likely better choices of crucible available.

A.4.3 Sputtering

Magnetron sputtering is a great method to deposit an amorphous thin film of just about any material needed. The three-target sputtering chamber used in this work was custom built by Professor Chia-Ling Chien's group at Johns Hopkins.

To sputter a material, a target 1-2 inches in diameter is loaded onto a cathode at the bottom of a vacuum chamber. The substrate to be coated is placed above the target on the anode. Once the system is at high vacuum, argon gas (or any inert gas) is introduced to the chamber. An argon plasma is ignited between the cathode (target) and anode (sample). The strong electric potential and magnetic field from permanent magnets placed under the target focus the plasma in a ring pattern on the face of the target. Argon ions bombard the target and target atoms are ejected toward the substrate mounted above.

The benefit of sputtering, as mentioned above, is that almost any metal can be sputtered with a DC plasma (RF plasma is used for insulating materials). Due to

APPENDIX A. FABRICATION DETAILS

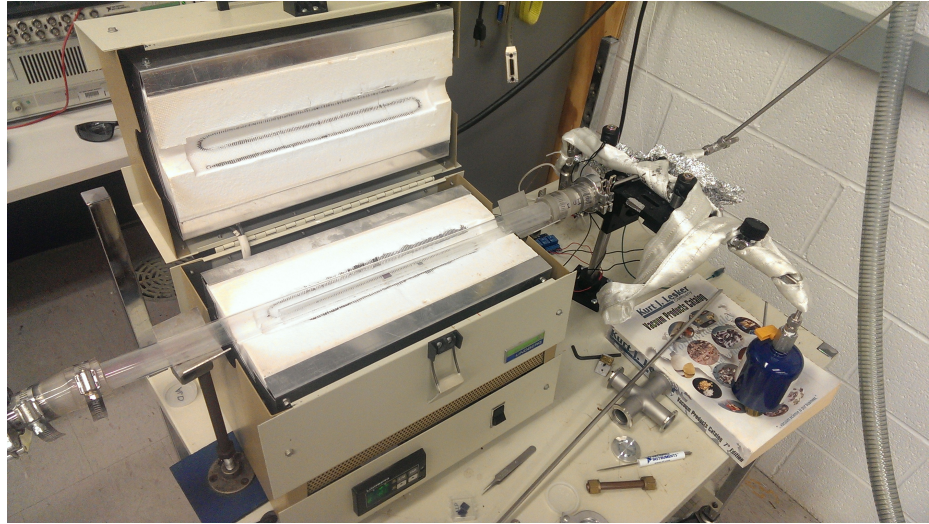


Figure A.5: The Markovic lab ALD reactor. Gas flow is from right to left.

the high energy of the argon ions and ejected target atoms, this method can damage some sensitive samples. There may be some evidence that this is the case with carbon nanotube samples. For this work, low energy plasma was used to keep the average energy of ejected target atoms around a few eV. This is about 10 times higher than the energies used in thermal and electron beam evaporation. Even if sputtering does introduce some damage to nanotube samples, it does not appear to be the primary source of disorder.

A.4.4 Atomic Layer Deposition

Atomic layer deposition (ALD) is a process in which thin, usually insulating, films are grown by reacting a series of gases. As a part of this work, we have constructed a homemade ALD reactor in the Markovic lab with the help of Streit Cunningham. It

APPENDIX A. FABRICATION DETAILS

uses the same Lindberg 1 inch tube furnace as the chemical vapor deposition setup.

Samples are loaded into a 1 inch quartz tube and placed in the furnace. The tube is evacuated to about 100 mTorr using a mechanical rough pump. A high purity N₂ flow is turned on and adjusted so the pressure in the chamber, with the pump still running, is 1000 mTorr. The N₂ flow will act as a carrier gas throughout the process. We have only tested the reactor for growth of Al₂O₃ layers. Two precursor gases are used in the growth of Al₂O₃, water vapor and trimethylaluminum (TMA). Once the quartz tube is evacuated and N₂ flow is set, the water vapor and TMA are alternately pulsed using computer controlled solenoid valves. Films grow one monolayer (1.1 Å) per pulse cycle. A typical recipe is as follows:

1. Evacuate tube to 100 mTorr with mechanical pump
2. Turn on N₂ flow such that the pressure reaches 1000 mTorr
3. Set furnace temperature to 130 °C
4. Pulse TMA for 1 second
5. Purge for 60 seconds
6. Pulse water for 1 second
7. Purge for 60 seconds
8. Repeat pulse/purge cycle until desired thickness has been reached

APPENDIX A. FABRICATION DETAILS

9. Cool furnace, turn off N₂ flow, turn off pump, remove sample

The goal with this recipe is to grow a quality insulating layer at a temperature low enough to be compatible with PMMA processing. This design is based on previous low temperature ALD growth by the George lab at the University of Colorado Boulder [24,25].

A.4.5 Liftoff

When patterning a thin film using a polymer mask, such as PMMA or S1813, the final step after deposition of the film is to remove the mask. This process is called liftoff, as the excess metal is lifted off the substrate along with the dissolved polymer mask.

Typically, liftoff is very simple. The sample is soaked in acetone for 1-12 hours (depending on what else is going on in the lab), then rinsed in IPA for 30 seconds followed by a 30 second rinse in water.

To help remove any stubborn material the sample can be sprayed with a bottle of acetone for a few seconds before rinsing in IPA. Some samples can also be placed in a beaker of acetone in a sonicator for a few seconds before rinsing in IPA. Sonication is not ideal for nanotube samples, as the process tends to break nanotubes off of the substrate and introduce defects in long tubes. An example of this can be seen in Figure A.6.

APPENDIX A. FABRICATION DETAILS

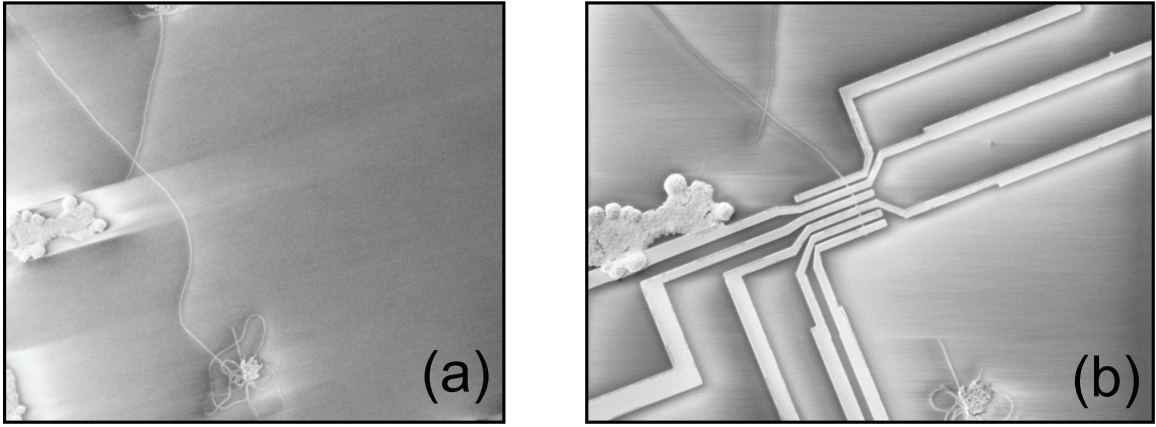


Figure A.6: (a) A substrate with catalyst islands and a few long nanotubes before patterning. (b) The same substrate after patterning and liftoff. Comparing the two images, it is clear that the use of sonication during liftoff has broken many of the nanotubes.

A.5 Room Temperature Testing

After devices have been fabricated, it is important to check the connectivity of the devices before spending the time to load samples into a cryostat.

A.5.1 Probe Station

The first step after fabrication is to test the resistance, and sometimes the gate behavior, of a device using a DC probe station. Our DC probe station was custom built for our lab and can be seen in Figure A.7.

The simplest and safest way found to check nanotube devices is to apply a small DC voltage (a few mV) between two of the large leads and measure the current with an ammeter. The measurements are done using a real-time LabView program. The bias is supplied by a National Instruments DAQ board through a 10^{-2} voltage divider.

APPENDIX A. FABRICATION DETAILS

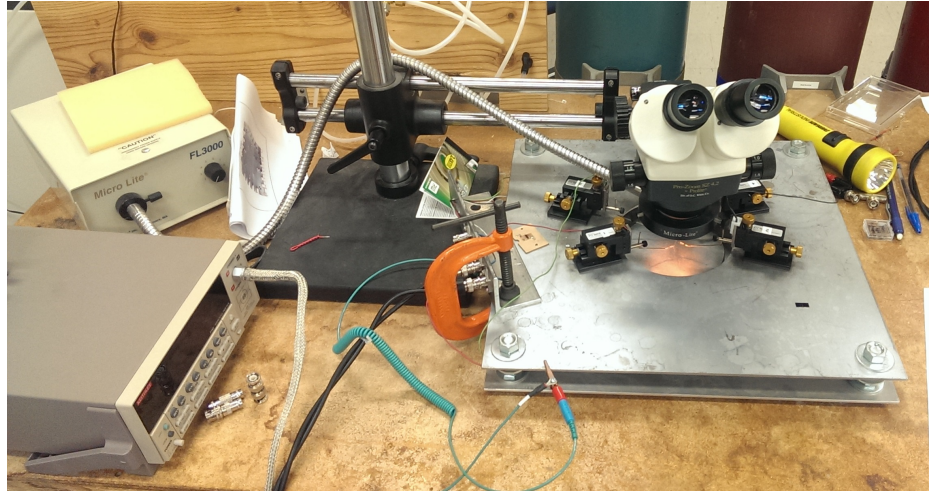


Figure A.7: The Markovic lab probe station. Four sharp probes are located under an optical microscope. Each can be connected to external sources and measurements using BNC connectors.

Current is measured by the same DAQ board by monitoring the output of an Ithaco 1211 current-to-voltage amplifier.

A.5.2 Wire Bonding

The final step in preparing devices for measurement is to wire bond the sample into a chip carrier. Each chip carrier is about 1 cm square and fits into a standard socket on each of our cryostats. The wire bonder is used to connect the large optical lithography leads on the sample to the chip carrier. An old Kulicke and Soffa wire bonder in Chia-Ling Chien's lab was used for this work. It can be seen in Figure A.8a.

The wire bonder is used to connect a point on the chip carrier to a point on the sample with an aluminum or gold thread. The thread is first pressed by the wire

APPENDIX A. FABRICATION DETAILS

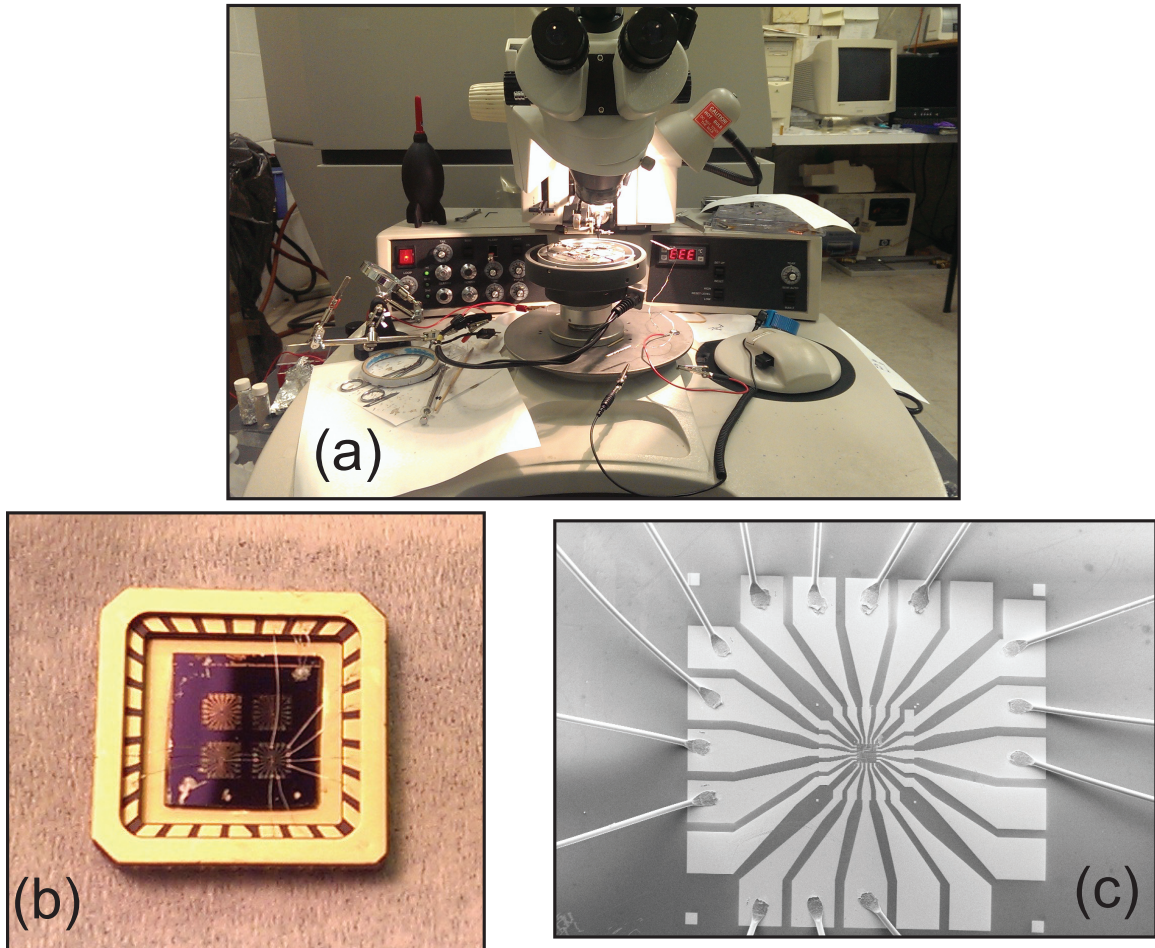


Figure A.8: (a) Kulicke and Soffa wire bonder. (b) An optical image of a completed device mounted in a chip carrier. (c) An SEM image detailing aluminum wires bonded to large gold leads.

APPENDIX A. FABRICATION DETAILS

bonder tip onto a bonding pad on the chip carrier. When the wire is in contact with the bonding pad the tip vibrates and presses down onto the sample to fix the wire into place. The tip can then be moved to contact one of the large optical lithography leads on the sample with the same wire. Once the second bond is made, the tip pulls away quickly to break the wire. The results of this process can be seen in Figures A.8b and c.

Appendix B

Measurement Details

A description of the cryogenics, measurement setup, and homemade electronics used in this thesis.

Bibliography

- [1] C. C. Wu, C. H. Liu, and Z. Zhong, “One-step direct transfer of pristine single-walled carbon nanotubes for functional nanoelectronics.” *Nano letters*, vol. 10, no. 3, pp. 1032–6, Mar. 2010. [Online]. Available: <http://www.ncbi.nlm.nih.gov/pubmed/20108926>
- [2] F. Pei, E. a. Laird, G. a. Steele, and L. P. Kouwenhoven, “Valley-spin blockade and spin resonance in carbon nanotubes.” *Nature nanotechnology*, vol. 7, no. 10, pp. 630–4, Oct. 2012. [Online]. Available: <http://www.ncbi.nlm.nih.gov/pubmed/23001302>
- [3] J. Kong, “Chemical vapor deposition of methane for single-walled carbon nanotubes,” *Chemical Physics Letters*, vol. 292, no. 4-6, pp. 567–574, Aug. 1998. [Online]. Available: <http://linkinghub.elsevier.com/retrieve/pii/S0009261498007453>
- [4] J. Kong, H. T. Soh, A. M. Cassell, C. F. Quate, and H. Dai, “Synthesis of

BIBLIOGRAPHY

- individual single-walled carbon nanotubes on patterned silicon wafers,” *Nature*, vol. 395, no. 3, pp. 878–881, 1998.
- [5] H. M. Aurich, “Carbon Nanotube Spin-Valve with Optimized Ferromagnetic Contacts,” Ph.D. dissertation, University of Basel, 2012.
- [6] L. L. Ouellette, “CHEMICAL AND BIOLOGICAL SENSING WITH CARBON NANOTUBES IN SOLUTION,” Ph.D. dissertation, Cornell University, 2008.
- [7] B. H. Hong, J. Y. Lee, T. Beetz, Y. Zhu, P. Kim, and K. S. Kim, “Quasi-continuous growth of ultralong carbon nanotube arrays.” *Journal of the American Chemical Society*, vol. 127, no. 44, pp. 15 336–7, Nov. 2005. [Online]. Available: <http://www.ncbi.nlm.nih.gov/pubmed/16262374>
- [8] M. J. Biercuk, N. Mason, and C. M. Marcus, “Local Gating of Carbon Nanotubes,” *Nano Letters*, vol. 4, no. 1, pp. 1–4, Jan. 2004. [Online]. Available: <http://pubs.acs.org/doi/abs/10.1021/nl034696g>
- [9] S. J. Kang, C. Kocabas, T. Ozel, M. Shim, N. Pimparkar, M. a. Alam, S. V. Rotkin, and J. a. Rogers, “High-performance electronics using dense, perfectly aligned arrays of single-walled carbon nanotubes.” *Nature nanotechnology*, vol. 2, no. 4, pp. 230–6, Apr. 2007. [Online]. Available: <http://www.ncbi.nlm.nih.gov/pubmed/18654268>
- [10] T. L. Dirks, “Tunneling Spectroscopy of Carbon Nanostructures: A Romance

BIBLIOGRAPHY

- in Many Dimensions,” Ph.D. dissertation, University of Illinois at Urbana-Champaign, 2010.
- [11] S. Huang, X. Cai, and J. Liu, “Growth of millimeter-long and horizontally aligned single-walled carbon nanotubes on flat substrates.” *Journal of the American Chemical Society*, vol. 125, no. 19, pp. 5636–7, May 2003. [Online]. Available: <http://www.ncbi.nlm.nih.gov/pubmed/12733894>
- [12] S. Huang, M. Woodson, R. Smalley, and J. Liu, “Growth Mechanism of Oriented Long Single Walled Carbon Nanotubes Using â’IJFast-Heatingâ’ Chemical Vapor Deposition Process,” *Nano Letters*, vol. 4, no. 6, pp. 1025–1028, Jun. 2004. [Online]. Available: <http://pubs.acs.org/doi/abs/10.1021/nl049691d>
- [13] R. Zhang, Y. Zhang, Q. Zhang, H. Xie, W. Qian, and F. Wei, “Growth of Half-Meter Long Carbon,” *ACS nano*, vol. 7, no. 7, pp. 6156–6161, 2013.
- [14] M. Bockrath, N. Markovic, A. Shepard, M. Tinkham, L. Gurevich, L. P. Kouwenhoven, M. W. Wu, and L. L. Sohn, “Scanned Conductance Microscopy of Carbon Nanotubes and λ -DNA,” *Nano Letters*, vol. 2, no. 3, pp. 187–190, Mar. 2002. [Online]. Available: <http://pubs.acs.org/doi/abs/10.1021/nl0100724>
- [15] T. S. Jespersen and J. Nygård, “Mapping of individual carbon nanotubes in polymer/nanotube composites using electrostatic force microscopy,” *Applied Physics Letters*, vol. 90, no. 18, p. 183108, 2007. [Online]. Available: <http://scitation.aip.org/content/aip/journal/apl/90/18/10.1063/1.2734920>

BIBLIOGRAPHY

- [16] T. Brintlinger, Y.-F. Chen, T. DuŁLrkop, E. Cobas, M. S. Fuhrer, J. D. Barry, and J. Melngailis, “Rapid imaging of nanotubes on insulating substrates,” *Applied Physics Letters*, vol. 81, no. 13, p. 2454, 2002. [Online]. Available: <http://scitation.aip.org/content/aip/journal/apl/81/13/10.1063/1.1509113>
- [17] S. Chaudhuri, S. Chatterjee, N. Katz, M. Nelson, and M. Goldbaum, “Detection of blood vessels in retinal images using two-dimensional matched filters.” *IEEE transactions on medical imaging*, vol. 8, no. 3, pp. 263–9, Jan. 1989. [Online]. Available: <http://www.ncbi.nlm.nih.gov/pubmed/18230524>
- [18] A. de Jesús Guerrero, Jose and Dalmau, Oscar and Alarcón, TeresaE. and Zamudio, “Frequency Filter Bank for Enhancing Carbon Nanotube Images,” in *Human-Inspired Computing and Its Applications*. Springer International Publishing, 2014, pp. 316–326. [Online]. Available: http://dx.doi.org/10.1007/978-3-319-13647-9_29
- [19] W. W. Hu, K. Sarveswaran, M. Lieberman, and G. H. Bernstein, “Sub-10 nm electron beam lithography using cold development of poly(methylmethacrylate),” *Journal of Vacuum Science & Technology B: Microelectronics and Nanometer Structures*, vol. 22, no. 4, p. 1711, 2004. [Online]. Available: <http://scitation.aip.org/content/avs/journal/jvstb/22/4/10.1116/1.1763897>
- [20] B. Cord, J. Lutkenhaus, and K. K. Berggren, “Optimal temperature for development of poly(methylmethacrylate),” *Journal of Vacuum Science &*

BIBLIOGRAPHY

- Technology B: Microelectronics and Nanometer Structures*, vol. 25, no. 6, p. 2013, 2007. [Online]. Available: <http://link.aip.org/link/JVTBD9/v25/i6/p2013/s1&Agg=doi>
- [21] S. Yasin, D. Hasko, and H. Ahmed, “Comparison of MIBK/IPA and water/IPA as PMMA developers for electron beam nanolithography,” *Microelectronic Engineering*, vol. 61-62, pp. 745–753, Jul. 2002. [Online]. Available: <http://linkinghub.elsevier.com/retrieve/pii/S0167931702004689>
- [22] M. J. Rooks, E. Kratschmer, R. Viswanathan, J. Katine, R. E. Fontana, and S. a. MacDonald, “Low stress development of poly(methylmethacrylate) for high aspect ratio structures,” *Journal of Vacuum Science & Technology B: Microelectronics and Nanometer Structures*, vol. 20, no. 6, p. 2937, 2002. [Online]. Available: <http://scitation.aip.org/content/avs/journal/jvstb/20/6/10.1116/1.1524971>
- [23] K. Koshelev, M. Ali Mohammad, T. Fito, K. L. Westra, S. K. Dew, and M. Stepanova, “Comparison between ZEP and PMMA resists for nanoscale electron beam lithography experimentally and by numerical modeling,” *Journal of Vacuum Science & Technology B: Microelectronics and Nanometer Structures*, vol. 29, no. 6, p. 06F306, 2011. [Online]. Available: <http://scitation.aip.org/content/avs/journal/jvstb/29/6/10.1116/1.3640794>
- [24] J. W. Elam, M. D. Groner, and S. M. George, “Viscous flow reactor with quartz

BIBLIOGRAPHY

- crystal microbalance for thin film growth by atomic layer deposition," *Review of Scientific Instruments*, vol. 73, no. 8, p. 2981, 2002. [Online]. Available: <http://scitation.aip.org/content/aip/journal/rsi/73/8/10.1063/1.1490410>
- [25] M. D. Groner, F. H. Fabreguette, J. W. Elam, and S. M. George, "Low-Temperature Al₂O₃ Atomic Layer Deposition," *Chemistry of Materials*, no. 16, pp. 639–645, 2003.

Vita

Nik did some physics. It could have gone better.